Nanoporous Conducting Materials

by

Alex Volosin

A Dissertation Presented in Partial Fulfillment
of the Requirements for the Degree
Doctor of Philosophy

Approved July 2012 by the
Graduate Supervisory Committee:

Dong-Kyun Seo, Chair
Daniel Buttry
John Devens Gust

ARIZONA STATE UNIVERSITY

August 2012

ABSTRACT

Nanoporous electrically conducting materials can be prepared with high specific pore volumes and surface areas which make them well-suited for a wide variety of technologies including separation, catalysis and owing to their conductivity, energy related applications like solar cells, batteries and capacitors. General synthetic methods for nanoporous conducting materials that exhibit fine property control as well as facility and efficiency in their implementation continue to be highly sought after.

Here, general methods for the synthesis of nanoporous conducting materials and their characterization are presented. Antimony-doped tin oxide (ATO), a transparent conducting oxide (TCO), and nanoporous conducting carbon can be prepared through the step-wise synthesis of interpenetrating inorganic/organic networks using well-established sol-gel methodology. The one-pot method produces an inorganic gel first that encompasses a solution of organic precursors. The surface of the inorganic gel subsequently catalyzes the formation of an organic gel network that interpenetrates throughout the inorganic gel network. These mutually supporting gel networks strengthen one another and allow for the use of evaporative drying methods and heat treatments that would usually destroy the porosity of an unsupported gel network. The composite gel is then selectively treated to either remove the organic network to provide a porous inorganic network, as is the case for antimony-doped tin oxide, or the inorganic network can be removed to generate a porous carbon material. The method

exhibits flexibility in that the pore structure of the final porous material can be modified through the variation of the synthetic conditions.

Additionally, porous carbons of hierarchical pore size distributions can be prepared by using wet alumina gel as a template dispersion medium and as a template itself. Alumina gels exhibit thixotropy, which is the ability of a solid to be sheared to a liquid state and upon removal of the shear force, return to a solid gel state. Alumina gels were prepared and blended with monomer solutions and sacrificial template particles to produce wet gel composites. These composites could then be treated to remove the alumina and template particles to generate hierarchically porous carbon.

DEDICATION

For Ellie “El Mercader del Dolor” Volosin

ACKNOWLEDGMENTS

I want to thank the Science Foundation of Arizona for providing me with my fellowship for my first few years of graduate school and also the Department of Energy for funding our Energy Frontier Research Center at ASU and my last few years of graduate school. Both have been instrumental in supporting my habits of research and living.

Also, thanks to all of my group-mates and collaborators for their assistance in helping me achieve my goals.

I also want to acknowledge my committee members who, among their many other commitments, found time and effort to contribute toward my success. Devens spearheaded our EFRC which provided funding and direction for so many, myself included. Dan was generous with his time to have many fruitful discussions with me that generated intriguing ideas and experiments and for that I am grateful. Of course, I want to thank Don for his understanding, insight, and patience. Especially his patience. I'm indebted to him for helping me to find the appropriate balance between optimism and pessimism in the laboratory and for showing me how to truly observe.

Thanks to my mom for not letting me forget that fundamentally, everything is magic, and my dad, for his rationality and wisdom and also my sister for a little bit of everything. Lastly, I want to thank my wife Ellie for putting up with my various hijinks and for supporting me through the series of trials and tribulations called graduate school.

TABLE OF CONTENTS

Page

LIST OF TABLES viii

LIST OF FIGURES ix

CHAPTER

1 INTRODUCTION 1

1.1 Conducting Materials 1

1.2 Porous Materials 3

1.3 Nanoporous Materials 5

1.4 Template Methods 10

1.4.1 Soft Templates 10

1.4.2 Hard Templates 12

1.5 Current Work 15

2 CHARACTERIZATION METHODS 18

2.1 Powder X-ray Diffraction 18

2.2 Raman 22

2.3 Gas Adsorption 24

2.4 Cyclic Voltammetry 26

2.5 Electron Microscopy 29

3 NANOPOROUS ANTIMONY-DOPED TIN OXIDE 31

3.1 Introduction 31

3.2 Experimental 34

3.2.1 Materials Synthesis 34

CHAPTER Page

3.2.2 Materials Characterization 37

3.3 Results and Discussion 40

3.4 Conclusion 57

4 MESOPOROUS CARBON 59

4.1 Introduction 59

4.2 Experimental 61

4.2.1 Mesoporous Carbon Preparation 61

4.2.2 Electrode Preparation 62

4.2.3 Materials Characterization 62

4.3 Results and Discussion 64

4.4 Conclusion 76

5 HIERARCHICALLY POROUS CARBON 78

5.1 Introduction 78

5.2 Experimental 80

5.2.1 Mesoporous Carbon Preparation 80

5.2.2 Hierarchically Porous Carbon Preparation 81

5.2.3 Materials Characterization 83

5.3 Results and Discussion 85

5.3.1 Mesoporous Carbon 85

5.3.2 Hierarchically Porous Carbon 101

CHAPTER Page

5.4 Conclusion 104

REFERENCES 106

LIST OF TABLES

Table Page

1. Surface areas and pore characteristics of the products. 36

2. Electrical resistivity at room temperature and the pore characteristics of selected pellet samples prepared under various pressures. 54

3. Surface area and pore characteristics of mesoporous carbon and ball-milled mesoporous carbon..... 67

4. Specific capacitances at listed scan rates and potentials. 74

5. Xerogel surface area and pore characteristics..... 86

6. Surface area and pore characteristics of MOCC materials..... 90

7. Surface area and pore characteristics for porous carbon samples. 97

8. Comparison of surface area and pore characteristics before and after template removal..... 104

LIST OF FIGURES

Figure Page

1. Unit cell of SnO_2. 2
2. Dense packing of percolating network of coronene molecules 5
3. Sol to gel transition 6
4. Several drying methods for wet gels 7
5. Self-organization of micellar templates to generate M41S type material 11
6. Using SBA-15 as a hard template 14
7. TEM image of CMK-3 ordered mesoporous carbon 15
8. Diffraction of an infinite crystal versus a finite crystal. 19
9. Hexagonal graphite and turbostratic graphite 22
10. Raman spectra for several carbons of varying crystallinity 23
11. Correlation of crystallite size with peak intensity ratio 24
12. Various types of gas adsorption isotherms as defined by IUPAC. 25
13. The double-layer 27
14. Various capacitive responses to a linear voltage sweep 28
15. Synthetic scheme of the mesoporous ATO materials. 40
16. ATR FT-IR spectra for ATO gel, R-F gel and ATO/R-F composite gel after drying. 42
17. TGA curves for ATO gel and ATO/R-F composite gel after drying. 43

Figure Page

18. Scanning electron microscope images of the sample L-6-4. The scale bars are 100 μm in (a) and 500 nm in (b)..... 45

19. Transmission electron microscope images of (a) M-3-4 (b) M-9-4 and (c) M-6-4 and (d) selected area electron diffraction (SAED) of M-3-4. 46

20. Powder XRD patterns of the M series with 0.4 *M* Sn precursor concentration with the simulated pattern of an ATO (11 at.% Sb, ICSD 41530). Silicon standard peaks are marked with stars. 47

21. N_2-sorption isotherms for M-0-4 (◆), M-3-4 (●), M-6-4 (▲), M-9-4 (■)..... 48

22. BJH pore size distributions for M-0-4 (◆), M-3-4 (●), M-6-4 (▲), M-9-4 (■). 49

23. N_2-sorption isotherms for 0-6-4 (■), L-6-4 (●), M-6-4 (▲), H-6-4 (◆)..... 50

24. BJH pore size distributions for 0-6-4 (■), L-6-4 (●), M-6-4 (▲), H-6-4 (◆). 52

25. XPS of the core level regions of Sn(3d) and Sb(3d) in as prepared M-6-4 sample. The deconvoluted peaks of $Sb^{5+}(3d_{3/2})$ and $Sb^{3+}(3d_{3/2})$ with binding energy peaks at 540.1 eV and 539.2 eV 53

Figure Page

26. BET surface area and total pore volume of M-6-4 pellets pressed at various pressures. 55

27. Temperature-dependent conductivity of M-6-4 pellet pressed at 2000 psi. 56

28. Kubelka-Munk transform of UV-Vis diffuse reflectance spectra for selected samples. 57

29. Nitrogen isotherms and BJH pore size distribution plots of the MOCC composite, mesoporous carbon, and the ball-milled mesoporous carbon. 64

30. TEM images of mesoporous carbon. 66

31. SEM image of a large piece of mesoporous carbon. 67

32. Thermogravimetric Analysis of mesoporous carbon after alumina removal. 68

33. Powder X-ray diffraction of mesoporous carbon and ball-milled carbon as compared to a calculated graphite pattern. 69

34. Raman spectra of mesoporous carbon and mesoporous ball-milled carbon 71

35. Cyclic voltammograms of the carbon tissue substrate and carbon black electrode. 72

Figure Page

36. Cyclic voltammograms of the ball-milled carbon electrodes in aqueous and organic electrolyte. 73

37. General synthetic method for porous carbon from thixotropic alumina gels. 85

38. Isotherms of xerogel composites X-1 (●), X-2 (■), X-3 (▲), X-4 (★), X-5 (◆). 87

39. BJH pore size distributions for X-1 (●), X-2 (■), X-3 (▲), X-4 (★), X-5 (◆). 88

40. Isotherms of MOCCs M-1 (●), M-2 (■), M-3 (▲), M-4 (★), M-5 (◆). 89

41. BJH pore size distributions of samples M-1 (●), M-2 (■), M-3 (▲), M-4 (★), M-5 (◆). 91

42. TEM images of (a) composite M-1, (b) porous alumina from burning M-1, and porous carbon C-1 at (c) high magnification and (d) low magnification. 92

43. Photograph of the resulting porous carbon pieces 93

44. SEM images of M-1 at (a) low magnification (b) high magnification, and the resulting porous carbon C-1 after alumina removal (c) and (d) 94

45. Thermogravimetric analysis of MOCC samples and carbon samples 95

Figure Page

46. Isotherms of carbon samples C-1 (●), C-2 (■), C-3 (▲), C-4 (★), C-5 (◆). 96

47. BJH pore size distributions for samples C-1 (●), C-2 (■), C-3 (▲), C-4 (★), C-5 (◆). 98

48. Raman data for carbons treated at different temperatures. 100

49. SEM images of hierarchically porous carbon and copper particle templates. 101

50. TEM of hierarchically porous carbon after removal of all templates. 102

51. N_2-sorption isotherms and BJH pore size distributions of the mesoporous (●) and hierarchically porous carbon samples (■)..... 103

CHAPTER 1

INTRODUCTION

1.1 Conducting Materials

In materials, multiple types of conduction exist, one of the most important being that of electrons, especially in our information age in which electronically conducting materials are essential. Metals are the most common electronically conductive materials (henceforth, conducting) and owe this property to highly delocalized electron density between atoms in the solid. Similarly, carbon, a non-metal, can exhibit conductivity in its graphite allotrope due to delocalized electrons existing in the pi-bonding orbitals of the layered graphite structure. Unlike metals however, conductivity in graphite is highly related to the crystalline order. Amorphous metal alloys exhibit resistivities as low as hundreds of micro-ohm centimeters, and liquid metals demonstrate resistivities only a few times greater than their crystalline counterparts. However in carbon, if the crystal order is disrupted, e.g. some sp^2-hybridized bonds in the carbon being reduced to sp^3, the conjugated network of pi-bonds that provides conductivity is disturbed. These graphite-like carbons of varying crystalline order are so called graphitic carbons and exhibit greater conductivity with more graphitic order, usually achieved through higher temperature treatment.[1,2]

Another group of materials exhibiting conductivity are transparent conducting oxides (TCOs). This paradoxical situation of transparency in the visible region and electronic conductivity exists in a group of transition metal oxides, generally doped, and are of great commercial importance. The most common is tin-doped

indium oxide (ITO) which exhibits excellent transparency and conductivity, but is limited by the rarity and ultimately cost of the predominant indium component.[3] Several alternatives exist in more earth-abundant elements such as tin oxide based materials. Tin(IV) oxide itself is an insulator when stoichiometric, but gains appreciable conductivity when non-stoichiometric, principally through oxygen defects.[4,5] The conductivity can be increased further by doping with electron donors like fluorine and antimony.[5–8] Tin(IV) oxide crystallizes in the rutile structure in space group $P4_2/mnm$ where the unit cell contains two formula units of SnO_2 and has tin atoms in body-centered arrangement with O atoms hexagonally close packed and coordinating the central tin atom to form chains of edge sharing octahedra. The unit cell can be seen in Figure 1 with the large spheres representing oxygen atoms and small spheres representing tin atoms.

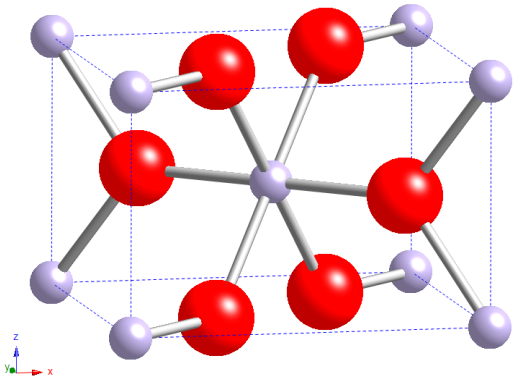

Figure 1. Unit cell of SnO_2 generated from data by Bolzan et al.[9]

When antimony is doped into tin oxide, the antimony replaces tin in the rutile structure and the structural change due to doping is minimal due to the similar size of tin and antimony.[6]

Conductivity is a particular functionality that is a desirable feature to have in materials and has been realized in many naturally occurring substances such as metals and graphite. The ever-advancing requirements in technology and science necessitate the addition of other functionalities like the generation of conducting materials that are also transparent to visible light. Imparting more desirable attributes to materials assists in realizing solutions to the problems mankind now faces.

1.2 Porous Materials

Porosity is an attribute that can be generated in materials that can enhance their functionality and application. These applications include those that involve solid/fluid interfaces such as catalysis,[10,11] energy devices like batteries, capacitors or fuel cells,[12,13] or material separation (filtration, chromatography, sieving)[14]. In porous materials, the manipulation of the quantity and availability of the solid is the parameter of variation. This variation is generally about finding a balance in the dichotomy between the "being" of the solid and the "nothingness" of the pore space.[15]

The key descriptive characteristics of porous materials are the surface area and pore volume (relative to another physical descriptor such as volume or mass) and the pore size. Generally speaking, to have more surface area of a particular material, one can simply acquire more of that material. A cube of matter of edge length 2 m has four times the surface of a cube of edge length 1 m. However, the 2 m cube uses eight times the amount of material as the 1 m cube. When the

amount of material is fixed, as in a 1 kg lump of clay, and topology is held constant, the surface area can be increased by increasing the anisotropy e.g. rolling a rod or pounding out a sheet. If topology is allowed to vary, the clay can be broken into small pieces and the surface area can be increased incredibly. Describing surface area is done relative to the material mass or volume which gives an indication to the efficiency of material usage with respect to surface area. An example of a real material exhibiting high anisotropy is graphene, which consists of a single layer of graphite. The specific surface area of graphene is generally reported as being 2630 m^2/g which is a theoretical value that applies to an infinite sheet of graphene. The specific surface area of finite graphene sheets is higher and increases with decreasing sheet size as more carbon atoms exist at sheet edges which provide more surface area relative to internal atoms in the sheet. This reduction in sheet size can continue into the size regime best described molecularly and the description of the specific surface area is akin to the philosophical exercise in assessing the surface area of a fluid. Sarkisov explored these molecular limits, but also addressed the specific surface area limits of porous materials. The model porous solid system chosen was a continuous percolating network of coronene molecules, shown in Figure 2, which are essentially small graphene platelets approximately 1 nm in diameter.

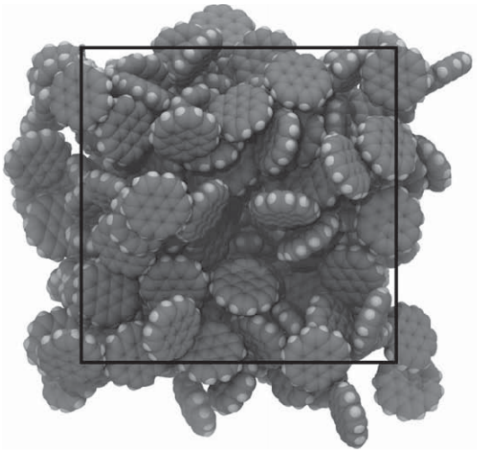

Figure 2. Unit cell of dense packing percolating network of coronene molecules, adapted from Sarkisov.[16]

The surface area for a continuous porous solid like the one in Figure 2 was calculated to be approximately 6400 m^2/g, which is much higher than that of graphene.[16] This demonstrates that as with nanoparticles, high specific surface areas are realized in porous materials with the development of nanoscale features.

1.3 Nanoporous materials

In the nanoscale regime, porous materials have several classifications of pore sizes. Micropores are defined as pores with walls opposite one another at a distance of less than 2 nm. Mesopores have opposing walls between 2 and 50 nm, with macropores defining pore sizes greater than 50 nm.[17] The term "nanoporous" is a broader description of porous materials in the nanoscale that include materials exhibiting micro-, meso- and/or macroporosity but are generally limited to pore sizes less than 100 nm.[18]

One of the most popular methods for synthesizing materials with inherent nanoporosity is the sol-gel method. This flexible method that can produce bulk

materials as well as thin films consists of two basic steps. Molecular precursors first react to form colloidal particles called a sol. These particles can then link together until a "percolation limit" is reached. This is when the linked particles span the volume of the solution and a gel is formed thus completing the second step, schematically shown in Figure 3.

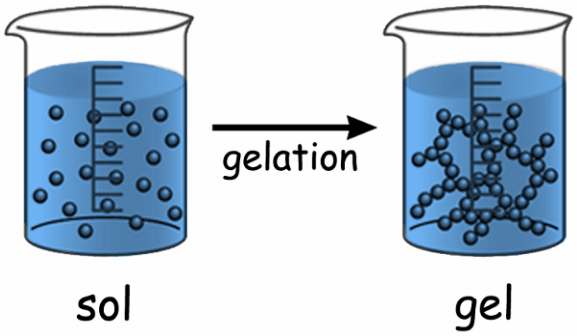

Figure 3. Sol to gel transition, adapted from Ladd et al.[19]

This gel consists of a small amount of solid that encompasses the solution in a tenuous and gossamer fashion.[20] At the removal of the liquid contained within the solid network, the empty space left behind constitutes the open porosity intrinsic to the sol-gel method.

There are several techniques to remove the pore liquid, the simplest being evaporative drying. A wet gel that is evaporatively dried at room temperature is termed a xerogel. The drying process causes tremendous shrinkage of the gel and collapsing of the pores due to the capillary forces caused by the receding liquid/vapor interface and generates a porous, but rather dense material as depicted in Figure 4.

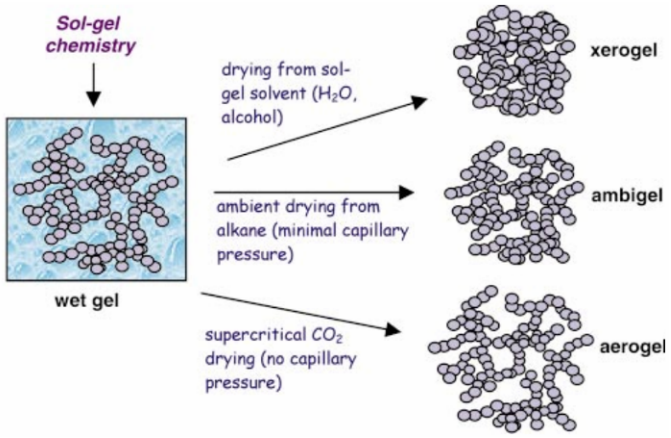

Figure 4. Several drying methods for wet gels, adapted from Rolison and Dunn.[21]

The drying method that best preserves the original solid network in the wet gel is the super-critical drying method. If the wet gel is brought to a temperature and pressure beyond the critical point of the pore liquid, the liquid/vapor interface no longer exists, and therefore the destructive capillary forces cannot act on the solid network. The system can then be depressurized to allow the removal of the exchanged fluid as a gas to generate an aerogel. Many solvents used in sol-gel syntheses have critical points at high temperatures and pressures, so in many cases it is preferable to exchange the pore liquid from the synthesis with one that has a critical point at lower relative temperatures and pressures, like carbon dioxide. At moderate pressure and temperatures below room temperature, carbon dioxide is a liquid that can be solvent-exchanged into a wet gel provided that the pore liquid is miscible with the non-polar carbon dioxide. Sometimes this requirement necessitates the exchange of the pore liquid used in gel synthesis (in many cases containing immiscible polar water) with a solvent miscible with liquid carbon dioxide like acetone or alcohol prior to the super-critical extraction. Some of the aerogels produced by this method are the lowest density solids in existence,

exhibiting porosities greater than 99 %, but this tremendous quantity of "nothingness" also dictates the brittle and easily friable nature of aerogels.[22] Not only this, the lengthy process is material and energy intensive. This has led to the development of several methods to circumvent the short-comings of aerogel preparation while still maintaining the inherently porous structure of gels.

The aerogel method preserves the porous structure by eliminating the liquid/vapor interface and thereby the destructive capillary forces. Other methods modify rather than eliminate the liquid/vapor interface, or change how the solid porous structure reacts to the capillary force. The capillary force exerted by the liquid on the solid network is proportional to the surface tension of the pore liquid.[20,21] Thus the pore liquid that was used to synthesize the gel can be exchanged for a liquid of lower surface tension to reduce the amount of shrinkage and pore collapse during ambient evaporative drying. This produces a material termed an ambigel that is much more porous than a xerogel, but less so than an aerogel. Other ambient methods include chemical modification of the gel surface and can allow for a "spring-back" of the gel after shrinking during evaporative drying.[23]

Of the many materials that can be synthesized through the sol-gel method, the preparation of silica gel is easily the most well characterized and understood process.[20] This is partly due to the relative stability of silica gel precursors, in particular silicon alkoxides, to hydrolysis. The transition metals are more electropositive than silicon making them more susceptible to nucleophilic attack.[24] This leads to much slower reaction rates for silicon alkoxides relative to

other transition metal alkoxides and provides for more facile control over the sol-gel process. Nevertheless, with careful control, many other transition metal oxides have been prepared using sol-gel chemistry[24] as well as mixed metal oxides like $MgAl_2O_4$[25] and doped metal oxides like antimony-doped tin oxide.[26]

The sol-gel method is also amenable to the preparation of non-oxide materials, such as the preparation of carbon materials from polymer gels.[27] While not sol-gel chemistry in the traditional sense, the polymer gels generated share many similarities with traditional sol-gel generated gels. Resorcinol (1,3 dihydroxybenzene) and formaldehyde can undergo condensation reactions to produce crosslinked polymer particles that can link covalently to generate polymer gels.[28,29] These generated gels consist of the same low solid and high liquid content as seen in inorganic gels and can undergo the same drying treatments as outlined above. The dried products can be pyrolyzed under reducing atmosphere to generate porous carbon materials.

While all of the above methods produce materials of high porosity, an important distinction to the methods is that the resulting porous solid is in most cases amorphous or poorly crystalline.[10,20] This is deleterious for conducting materials like TCOs and carbons which require crystallinity to exhibit good conductivity. This can be addressed by calcination at high temperature which provides for crystallization and sintering of the solids, enhancing the mechanical properties, but at the expense of the open porous architecture granted by the sol-gel process.[21] Post-synthetic calcination also complicates the control of the final

pore size of the final porous material, especially in the cases where large volume changes occur during the process.

1.4 Template Methods

1.4.1 Soft Templates

For better control over the final porous structure of sol-gel derived materials, many groups have employed the use of templates for pore generation. Templates are temporary materials incorporated at the beginning of the sol-gel preparation and are subsequently removed at the end to provide pore space. The pore morphology and size generated by the template is determined by the dimensions of the template. Templates can be divided into two general classes: soft and hard. Soft templates are generally molecular or polymer components that are included in a reaction mixture and phase separate during material processing. Many of the most popular templates can self-organize into ordered structures which the desired material (usually oxide gels) can form around. Upon removal, the templates leave behind regular ordered pores of controllable size. The M41S family of mesoporous aluminosilicate materials employs the use of a quaternary ammonium salt with a long hydrocarbon tail. The ammonium salt acts as a surfactant and at appropriate concentrations can form cylindrical micelles. These micelles self-organize into a hexagonal packing arrangement and thusly produce pores of the same type. This self-organization is demonstrated in Figure 5.

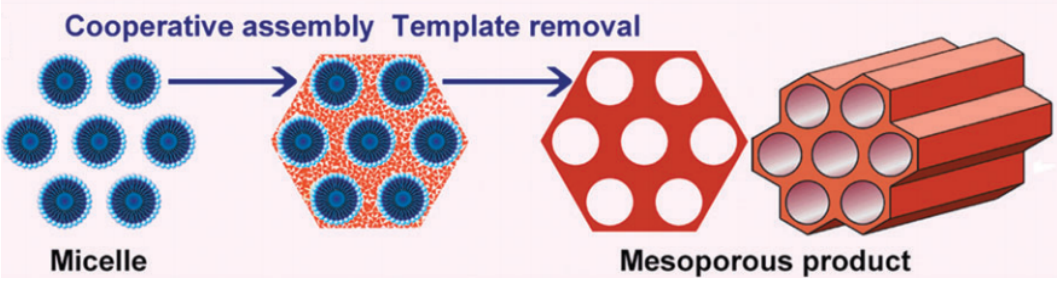

Figure 5. Self-organization of micellar templates to generate M41S type material, adapted from Shi et al.[30]

With adjustment to the hydrocarbon tail of the quaternary ammonium salts, micelles and subsequently pores of various sizes can be produced.[31,32] Materials of similar geometry can be prepared with block co-polymers as the structure directing agents as in mesoporous silica SBA-15.[33,34] These methods are quite flexible and general in their application and have been used to generate a wide variety of conducting materials. Tin oxide[35] has been prepared with ordered cylindrical mesopores using these methods as well as TCOs like ITO[36] and doped tin oxides[37,38]. These materials exhibit well-ordered porosity but other soft templates like polymers can be used to generate random porosity as well.[12] In O'Regan and Grätzel's seminal work in preparing TiO_2 thin films for dye-sensitized solar cells, they used polyethylene glycol polymer as a soft template to arrange preformed titania crystallites into a percolating porous network.[39] Porous carbons have also been prepared using soft templates in a similar manner. Zhao and coworkers prepared hexagonal ordered cylindrical mesoporous carbons from block co-polymer soft templates and phenol-formaldehyde resol as the carbon source.[40,41] This can be challenging in its application because the method relies on the ability of the soft template to decompose with low carbon residue and the

desired porous carbon to remain stable with high carbon residue during pyrolysis, which strongly limits the selection of materials that can be used.[42]

Soft template methods can generate a wide variety of mesoporous materials but some suffer from a few inherent problems. Many soft-templated ordered mesoporous materials use block co-polymers which are specialty chemicals that are relatively expensive and volatilized upon decomposition, therefore having no possibility of reuse. Additionally, the amorphous porous materials faithfully replicate the self-assembled micellular structure formed by the soft-templates, but upon calcination or pyrolysis, the resulting porous solid exhibits pores that have shrunk considerably with thickened pore walls.[41,43,44]

1.4.2 Hard Templates

Hard templates are solid materials that are either dispersed particles or fibers into a precursor solution or an existing porous material that can be infiltrated with a precursor solution to generate a negative replica. Colloidal silica particles are a popular hard template material especially for porous carbon formation because the silica can be easily removed in a chemical etching step with hydrofluoric acid.[45,46] Because the templates are not necessarily volatilized, there is a possibility of recovering and regenerating the silaceous template from the etchant solution. This simple dispersal of particles generally produces disordered porous materials with the pore size and volume being determined by the colloid size and concentration respectively. Because these particles are dispersed, the controlled porosity introduced by the template particles is not necessarily continuous

throughout the solid. This can be addressed when the spheres are prepared in a close-packing arrangement by filtration, centrifugation or sedimentation to generate ordered porous materials with continuous open porosity. This so-called opal structure is then infiltrated with a precursor solution that is then reacted to form an inverse-opal structure upon removal of the opal template.[47] This method is applicable to the generation of large mesopores and macropores in carbons[48] and many metal oxides[49] including ATO[50]. Producing opals can be time consuming and limiting in the amount of material that can be batch processed. Additionally, opals are limited to large particle sizes that can easily filtered, centrifuged or sedimented, thus limiting the size of pores that can be generated.

Using an existing porous material as a hard template can allow the production of smaller feature sizes than preformed particles while additionally providing a continuous template without extra processing steps. Soft-templated silicas like SBA-15 have been used as hard templates for the synthesis of other porous materials. It would be expected that using a porous material with ordered cylindrical pores as a template would generate collections of nanofibers or nanorods as a resulting replica. However, it was determined that the templated cylindrical mesopores in SBA-15 are connected randomly by small micropores and this allows a templated material to become a continuous solid as shown in Figure 6.[51]

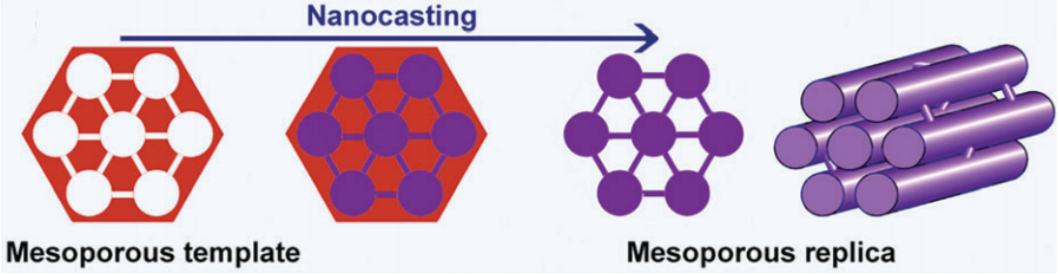

Figure 6. Using SBA-15 as a hard template, adapted from Shi et al.[30]

SBA-15 has been used as a template for the synthesis of ordered mesoporous tin oxide for applications in batteries[52] and solar cells[53]. While a variety of metal oxides have been prepared using hard templates of silica, the method in general is limited by the stability of the target porous metal oxide; it has to withstand the harsh HF or NaOH etching step for the removal of the silica template.[54] However this limitation in the production of porous metal oxides from porous silica templates is an advantage for the production of porous carbons from the same. Carbon is very stable across a wide range of pH conditions and thus can withstand the chemical etching step required for porous hard template removal. Whole families of ordered mesoporous carbons have also been generated from the vast array of porous silaceous templates, such as the use of SBA-15 to generate ordered porous carbon CMK-3, shown in Figure 7.[55]

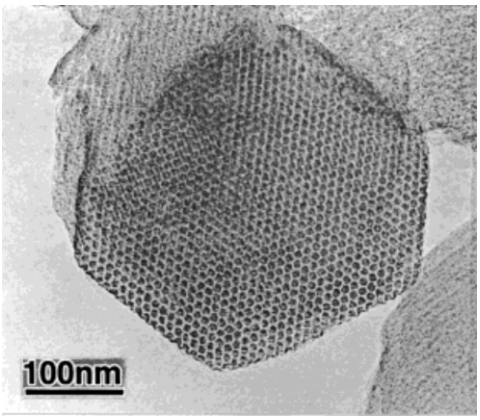

Figure 7. TEM image of CMK-3 ordered mesoporous carbon, adapted from Jun et al.[55]

The use of hard templates for porous material production is a flexible and widely applied method, though it is limited in several ways. Discrete particles can be used, but require special pre-treatment to ensure close packing of the template and that a continuous porosity can be generated upon removal. These pre-treatments are only effective on particles of large size and thus the resulting porosity is generally limited to macropores and very large mesopores.[47] The use of existing porous materials as hard templates such as SBA-15 is also difficult because in many cases, multiple infiltrations of the desired precursor are necessary to generate a continuous templated material.[52,55,56] When these time consuming iterative infiltrations are accounted for in addition to the lengthy preparation time of the porous template, the technique is further devalued.

1.5 Current Work

The work presented in this thesis outlines several techniques for the preparation of nanoporous conducting materials while being scalable and

remaining cost-effective. The existing methods described previously can suffer from several problems:

1. Excessive shrinkage and densification can occur during processing, especially in non-templating methods.
2. Many soft templates are expensive and non reusable, and hard templates require preparations that in many cases use soft templates.
3. Precursor infiltration into porous hard templates is required for effective continuity of the final templated material.

Herein, methods are presented that employ the use of interpenetrating networks of wet gels and *in-situ* generated polymers as sacrificial templates for synthesizing nanoporous conducting carbons and transparent conducting oxides. These methods address the problems of contemporary methods in the following ways:

1. The interpenetrating networks strengthen and buttress one another against shrinkage during drying and calcination to preserve porosity and allow for the use of energy-efficient ambient drying techniques
2. The inorganic component used as a template can be reused and regenerated easily. The organic component as a template is more cost-effective relative to existing popular templates.
3. Template infiltration is not required due to the *in-situ* formation of the organic component. Due to the interpenetrating architecture of the inorganic and organic networks, continuity of the solids is assured which is essential for conducting materials.

The use of interpenetrating networks of inorganic and organic gels is a cost and energy efficient method for the scalable production of highly porous materials that exhibit electrical conductivity. It is shown herein that this method can be used to produce nanoporous conducting carbons and transparent conducting oxides.

CHAPTER 2

CHARACTERIZATION METHODS

2.1 Powder X-ray Diffraction

X-ray diffraction is a well-established technique for the determination of atomic structure in crystalline materials. In crystalline materials, atoms are arranged in relatively simple patterns that repeat throughout 3-dimensional space. Diffraction, as a general phenomenon, occurs when waves encounter a regularly spaced set of scattering objects. Atoms are scattering objects, because the electrons surrounding atoms are able to absorb and reemit electromagnetic radiation in directions not necessarily equal to the direction of the incident radiation. Diffraction would be expected to occur in a collection of regularly spaced atoms like a crystal provided that the wavelength of impinging radiation is of a similar magnitude to the regular spacing between the constituent atoms. Many inter-atomic distances in crystalline materials are on the order of a few Angstroms, so an appropriate wavelength of electromagnetic radiation for diffraction in crystals is found in the range of X-rays near 0.5-2.5 Å.[57]

X-ray diffraction is a well-established technique for the determination of atomic structure in crystalline materials. It is a non-destructive method for phase determination of single crystals as well as polycrystalline or powdered crystals. In addition, X-ray diffraction can be used to approximate the primary crystallite size of a material through the implementation of Scherrer's equation

$$B = \frac{K\lambda}{t\cos\theta} \qquad (1)$$

where B is the width of the diffraction line at half of the maximum intensity in radians, K is Scherrer's constant (which can be approximated to be 1 for spherical crystallites), λ is the wavelength of the X-ray source (most commonly 1.5418Å, that of Cu Kα radiation), t is the diameter or thickness of the crystallite, and θ is the angle of reflection of the diffraction line in question. In the case of an infinite crystal, line width is not observed and only the angle that satisfies the Bragg condition provides diffraction intensity as shown in Figure 8a, adapted from Cullity.[57] However, line width is present in samples measured by X-ray diffraction due to the finite size of the crystalline material as shown in Figure 8b.

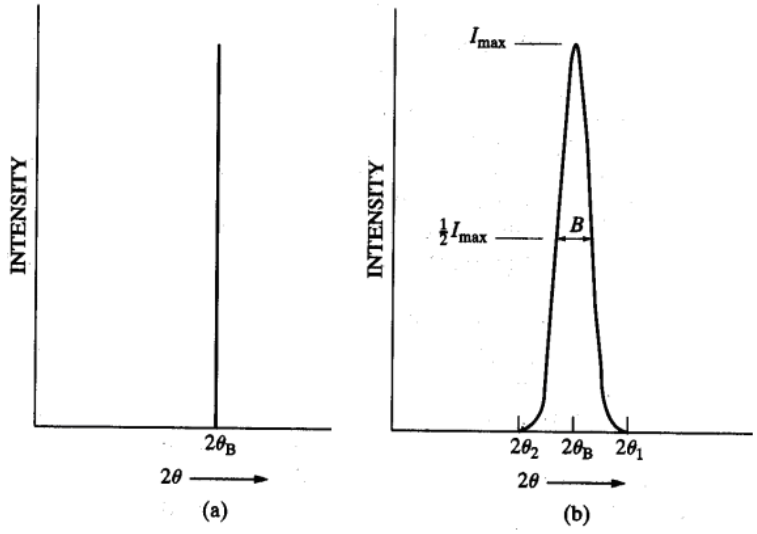

Figure 8. Diffraction of an infinite crystal versus a finite crystal.

Bragg's Law is satisfied when an incident wave front interaction at a particular angle with parallel diffracting planes of a particular inter-plane spacing results in path differences in the parallel waves to provide for constructive interference with one another. At other diffracting angles not satisfying the Bragg condition, the waves interfere destructively and provide no signal intensity. In the case of

angles that vary only slightly from satisfying the Bragg condition, the diffracting planes that provide the destructive interference lie deep within a crystal, which means for a finite crystal, they may not exist at all. This results in angles of diffraction that do not satisfy Bragg's Law but still provide measurable diffraction intensity near Bragg angles due to incomplete destructive interference as a finite crystal size effect. This range of angles is represented by $2\theta_1$ and $2\theta_2$ in Figure 8b. However, crystal size is not the only source of line broadening; many instrumental and other sample parameters can contribute to line width. Various corrective factors to the line width B can be applied, but because the estimation of crystallite size employs the measurement of the width of the diffraction line B, there are limitations on the size of crystal imposed by the accuracy of these corrective methods. At large crystallite sizes, which correspond to narrow line widths, the width of the diffracting line is more strongly influenced by the experimental arrangement and other material parameters than the crystallite size. This sets a practical maximum particle size at around 200 nm while implementing advanced techniques and corrective factors. Crude measurements can give reasonable estimations of crystallite size in the range of 50-100 nm.[57] A minimum crystallite size that can be identified with reasonable confidence using this method is around 10 nm, where a normal diffraction maximum is not achievable and the background signal has a significant presence in the broad diffraction line of the nanocrystallite.[58]

Materials synthesized under varying conditions can exhibit different degrees of crystallinity and powder X-ray diffraction is an effective tool to indicate this

degree of crystallinity. Materials can range from amorphous materials that give no diffraction at all up to large single crystals which give sharp and intense diffraction lines. This range of phases can be represented by various types of carbon which span these two extremes of atomic ordering. Amorphous carbon is observable in carbonaceous materials treated at low temperature such as soot. These carbons still contain some short range ordering in terms of local bonding of sp^2 and sp^3, but these domains are not large enough to construct diffracting planes to cause distinguishable diffraction lines in a collected pattern. Pure crystalline graphite is a very different allotrope and contains layers of sp^2 hybridized carbons that stack in a registered ABAB or ABCABC pattern for hexagonal (Figure 9) and rhombohedral graphite respectively.[59] Graphite carbon produces an X-ray diffraction pattern with many diffraction lines in great contrast to the amorphous carbon. Carbon materials that lie in the intermediary of amorphous and perfectly crystalline contain graphite layers of predominantly sp^2 hybridized carbon and are arranged in a layered structure, but there is not an ABAB stacking pattern, and there need not be a stacking pattern at all. These graphitic carbons with stacked layers that are rotated randomly relative to one another are termed "turbostratic" graphite[60] and can be viewed in Figure 9. These types of graphite only produce a single diffraction line that corresponds to the graphite layers stacked in the crystallographic c direction. No other diffracting planes arise because no long range ordering occurs between carbons from different graphite layers to form a coherent diffracting plane.

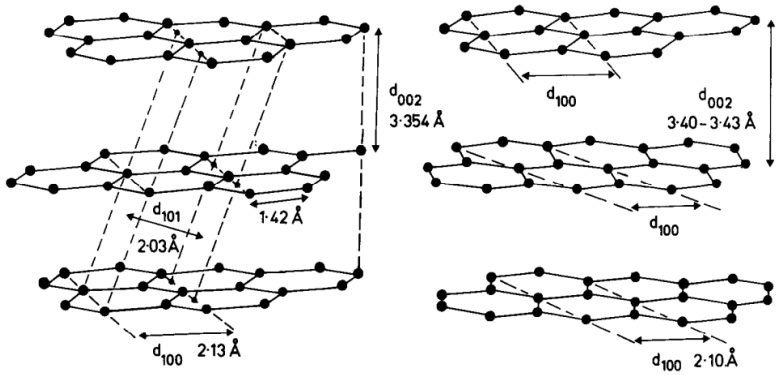

Figure 9. Hexagonal graphite and turbostratic graphite adapted from Knox.[14]

Scherrer's equation can also be applied as a method for investigating the crystallite size of carbons of varying graphitic character. The crystallite size in the crystallographic *c* direction, L_c, (average thickness of the stacked graphite layers) can be calculated from the (*00l*) reflections. If they are present, the (*hk*) reflections can be used to calculate an average diameter of the crystallites parallel to the stacked layers, L_a.[1] However, different Scherrer's constants are required due to the anisotropy of graphite crystallites. For calculating L_c a value of K = 0.89, and for L_a a value of K =1.84 is appropriate.[59]

2.2 Raman

Raman spectrometry is a non-destructive technique used for chemical bond characterization as well as chemical identification. At the advent of the technique, predominantly liquid and gas samples were analyzed and the applications of Raman spectroscopy of solids were not fully realized until the development of lasers and techniques to avoid fluorescence.[61] For carbon materials, Raman spectroscopy has become an indispensable characterization tool especially for

identifying the extent of crystallinity in widely varying graphitic carbons. Figure 10 shows Raman spectra of several carbon samples, some of high crystallinity, and others that are poorly crystalline or amorphous, as adapted from Knight and White.[62]

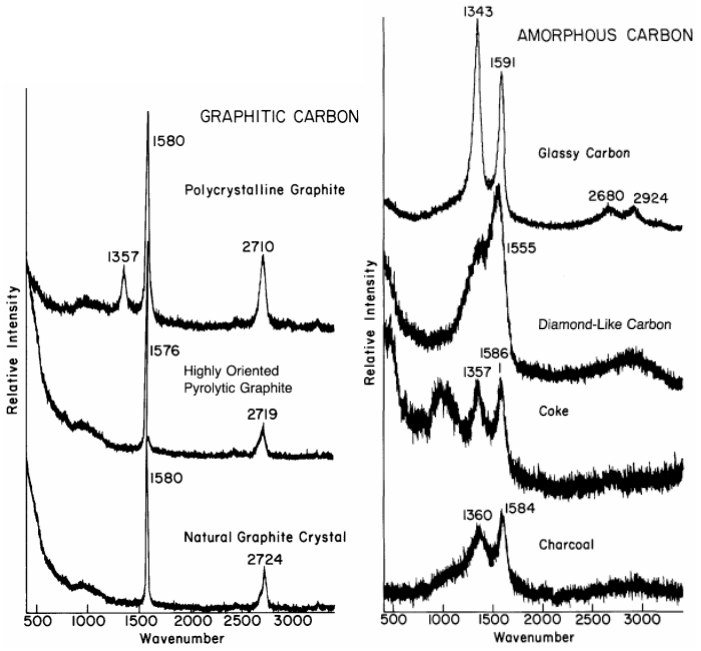

Figure 10. Raman spectra for several carbons of varying crystallinity

The most notable features in the spectra (with respect to crystallinity) are the bands near 1360 and 1580 cm^{-1} which are the so called D and G bands respectively. The D band appears in samples of less than perfect crystalline order, and the G band is present in essentially all carbon samples with some graphitic character. The G band has been shown to correlate with an in-plane stretching mode within the graphite sheets, and this assignment is well established in the literature.[62–64] For the D band, Tuinstra and Koenig proposed that a particular vibrational mode that is Raman inactive on an infinite graphite sheet becomes

active when the graphite sheets become finite.[64] It has been shown that the intensities of the G and D bands present in the Raman spectrum of a carbon sample can be used for estimating the graphite crystallite size as shown in Figure 11 adapted from Tuinstra and Koenig.[64]

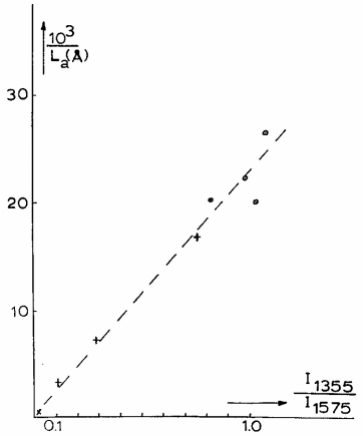

Figure 11. Correlation of crystallite size with peak intensity ratio

2.3 Gas Adsorption

Gas adsorption is a well established and non-destructive technique used to characterize the surface area and pore features of solids. The essence of the technique relies on admitting a known quantity of gas to a clean and dry solid sample and deducing the amount adsorbed on the surface by a change in weight of the sample or the measured pressure of the remaining unadsorbed gas. A series of measurements at different pressures and constant temperature are made and collected into a data set called an isotherm. A collection of isotherms as defined by IUPAC is given in Figure 12, as adapted from Sing, et al.[17]

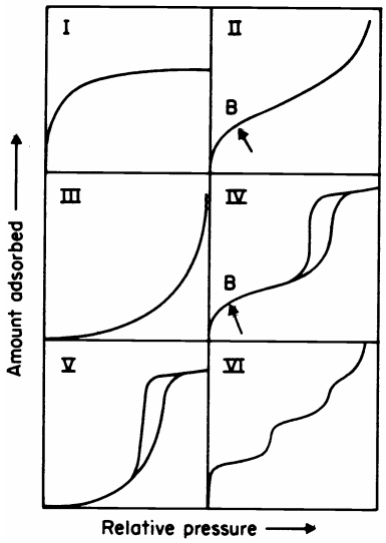

Figure 12. Various types of gas adsorption isotherms as defined by IUPAC.

The extraction of the surface area and pore characteristics from the collected isotherm relies on the application of various models. The BET equation[65] is the most popular model for determining the surface area of a material, and remains so after more than 70 years due to its ease of use and applicability to a wide variety of solids and adsorption gases.

$$\frac{p}{n^a(p_o - p)} = \frac{1}{n_m^a C} + \frac{(C-1)}{n_m^a C} \cdot \frac{p}{p_o} \qquad (2)$$

In equation 2, n^a is the amount adsorbed at the relative pressure p/p_o, n_m^a is the monolayer capacity and C is the BET constant. The linear plot generated according to this equation can be used to determine the monolayer capacity, which with the physical dimensions of the adsorbed gas, a surface area of the material can be calculated.

The types and quantities of pores present in a solid can also be characterized based on the collected isotherm. One popular model for characterizing mesopores

and small macropores in particular is the BJH model.[66] This model is based on the modified Kelvin equation which correlates the thermodynamic stability of a meniscus inside a cylindrical pore with the gas pressure at the interface. In the isotherm, the quantity of gas desorbed between data points can be correlated with a cylindrical pore of a particular size that thermodynamically support a meniscus of adsorbed gas. Several of the assumptions of the model, especially when disordered porous solids are analyzed, are not correct, but nonetheless, useful relative comparisons in series of similarly ordered structures can be made.[67]

2.4 Cyclicvoltammetry

Cyclic voltammetry is a solution based electrochemical method implemented by measuring current responses of an electrode with an applied linear change in electric potential. This method is sensitive to currents arising from faradaic processes, where electrons transfer across the electrode/solution interface and partake in chemical and oxidative changes, as well as non-faradaic processes, where charges accumulate at an electrode surface. This collection of charges at the electrode causes an accumulation of opposite charges from ions in the solution around the electrode to form the so called double-layer as depicted in Figure 13.

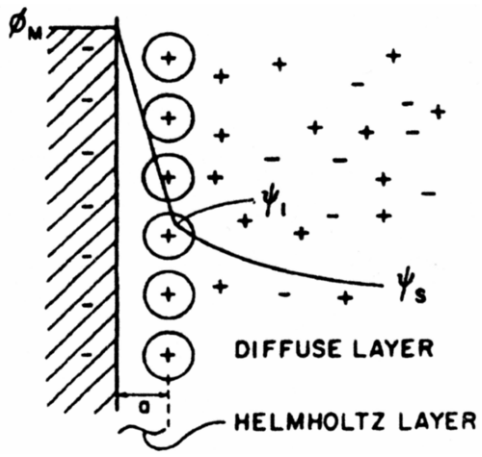

Figure 13. The double-layer, adapted from Conway.[68]

This phenomena is the basis for the capacitance in electrochemical double layer capacitors (EDLCs). Capacitance for a single electrode is proportional to the surface area of the electrode and inversely proportional to the thickness of the double layer (represented by "a" in Figure 13) which is usually less than 1 nm.[69] Cyclic voltammetry is a very sensitive method for investigating the double layer in high surface area EDLCs and determining the capacitance.

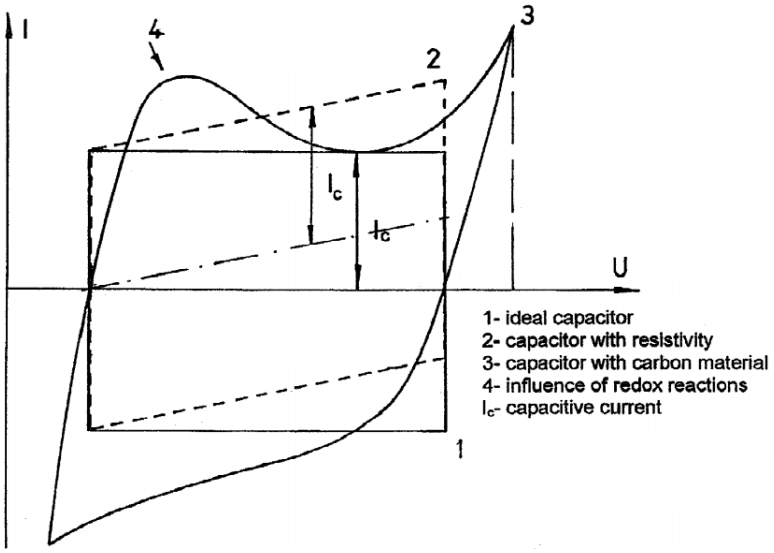

Figure 14. Various capacitive responses to a linear voltage sweep, adapted from Frackowiak and Béguin.[70]

Figure 14 depicts cyclic voltammograms for several types of capacitors. Cycle 1 is an ideal capacitor that exhibits a current response that is independent of potential. Cycle 2 exhibits a resistive response to the applied potential sweep in addition to a capacitive response. Cycle 3 is an example voltammogram from a carbon material that exhibits a non-faradaic capacitive response as well as some faradaic processes. The capacitive currents labeled I_c in Figure 14 can be used to calculate a capacitance C with the potential scan rate s according to

$$C = \frac{I_c}{s} \qquad (3)$$

Specific capacitances can then also be calculated by normalizing the measured capacitance over the active electrode mass or volume.

2.5 Electron Microscopy

Electron microscopy is a high-vacuum non-destructive technique that is useful in its most basic application as an imaging method that surpasses the resolution limit imposed by the physics of light. The resolution limit of an incident beam is proportional to the wavelength, and thus the resolution limit of optical microscopy is dictated by the shortest wavelengths of visible light of about 400 nm and a resolution of about 0.2 μm.[71] However, electrons exhibit wavelengths on the order of tenths of angstroms and can provide resolutions on the order of 2-5 angstroms.[72]

Two of the most popular electron microscopy techniques are transmission (TEM) and scanning (SEM) electron microscopy. Both techniques use accelerated electrons that impinge upon a sample, but each method generally measures a different type of signal and generates an image in a different way. Accelerating voltages are much larger for TEM and electrons in the beam are therefore traveling much faster. Wavelength is inversely proportional to momentum, so faster electrons have shorter wavelengths, and it follows that TEM has a smaller resolution. TEM uses a flood beam and a series of lenses, much like an optical microscope, to focus an image created by transmitted electrons (elastically and inelastically scattered). Because the electrons used for imaging are transmitted through the sample, thin samples are required; general morphology can be examined with thicknesses on the order of 1 μm, but high resolution imaging requires samples of less than 50 nm.[72]

SEM uses much lower accelerating voltages and therefore exhibits larger resolution. The beam used for SEM is a narrowly focused beam that rasters across the sample. The incident beam of electrons can ionize the atoms of the sample which can excite loosely bound valence or conduction electrons. Provided they have enough kinetic energy, these secondary electrons can be emitted from the surface and collected to generate an image. Additionally, the electron beam can be elastically scattered at high angle to generate an image of so-called backscattered electrons. The image forming signal is not transmitted through the sample, so there is no requirement for thin samples as in TEM. However, for high resolution imaging, the samples must be electrically conductive to prevent charging of the sample surface and image distortion. SEM can be used to image samples in the same range as optical microscopy, but can easily image features on the scale of tens of nanometers.[71]

CHAPTER 3

NANOPOROUS ANTIMONY-DOPED TIN OXIDE

3.1 Introduction

Mesoporous metal oxide materials have been extensively studied because of their potential chemical applications such as heterogeneous catalysis.[10,11] More recently, their potential applications have been extended to photoelectrochemical solar cell fabrications,[73] biosensors,[74] and electrooptical devices[37] where transparent conducting oxides (TCOs) play a critical role. Antimony-doped tin oxide (ATO), a crystalline material, has been emerging as an important TCO material because of the cost benefit in comparison to indium tin oxide (ITO).[3] Synthesis of mesoporous ATO materials has been reported by the liquid crystal template method[37,38] and it was shown that they could be used as high surface-area electrode substrate in fabrication of electroluminescence devices.[37] In other work, highly-conductive mesoporous ATO has been produced by first synthesizing ATO nanoparticles through a sol-gel route and subsequently using a block-copolymer soft template.[75] In general, control of pore sizes would require templates with different molecular sizes for the templating methods. Disordering of pore channels and the one-dimensional (1D) nature of the pore opening could hamper efficient absorption of active molecules.[37]

Among other synthetic methods, the sol-gel process is convenient to provide highly mesoporous metal oxides that have three-dimensionally (3D) interconnected gel network structures of nanoparticles with a textural porosity.[10,21] However, one challenge in the sol-gel approach is that during the drying and

calcination of the gels the pore structures often collapse and thus limit the control of pore sizes.[21] This is particularly the case for nonsilicate crystalline metal oxides, such as ATO, for which the amorphous hydrous metal oxide gels need to be dehydrated and crystallized by heating, causing drastic atomic rearrangements.[21,75] The problem is also common with the liquid crystal template approach, although it can be alleviated when the calcination is carried out at relatively low temperatures or the synthesis utilizes structurally more robust but often rare template molecules.[44,76] For mesoporous ATO production, challenges in using commercially available template polymers have been recognized due to the peculiarity of tin chemistry.[75]

In an alternative approach, employment of sacrificial hard templates (nanocasting method) has been successful in providing mesoporous structures of various metal oxides that often require high temperature calcination.[77,78] The interconnectivity of the pores in the metal oxide products is ensured when the templates have a continuous network structure. Especially, porous carbon templates with three-dimensionally interconnected network structures, like carbon aerogels,[78] can provide highly mesoporous metal oxides with 3D interconnected pore networks. However, the method can be less convenient because the templates must be prepared prior to the metal oxide synthesis, especially when variation of pore sizes is necessary. In addition, the infiltration of the metal oxide precursor needs to be carried out often multiple times in order to avoid disconnection of the metal oxide network structure in the final product material. Therefore, the development of a simple method for production of highly open

mesoporous TCOs with a convenient control of pore characteristics is still desirable.

By combining the advantages of the sol-gel and nanocasting methods, it is report herein a simple *one-pot* sol-gel synthesis of highly mesoporous antimony-doped tin oxide (ATO) materials with a 3D interconnected pore network structure by *sequential formation* of interpenetrating inorganic and polymer gel networks the latter of which serves as a hard template. The materials exhibit controlled pore sizes by simply varying the precursor concentrations. In the literature, interpenetrating inorganic-polymer network structures have been realized in a one-pot process by premixing inorganic gel precursors and organic polymer gel precursors in a solution and then promoting "concurrent" gelation of both inorganic gel precursors and organic polymer gel precursors in the solution.[79–81] In this synthetic procedure, the hydrolysis, polycondensation, and polymerization occur concurrently among the precursors in the solution and can be catalyzed by a common acid that is added to the solution together with the precursors.[79] Various mesoporous carbon-metal or carbon-metal oxide composites have been prepared through this method upon pyrolysis of the inorganic-polymer composite gels.[80,81] For example, it has been shown that CuO/resorcinol-formaldehyde gels can be prepared by two gelation reactions occurring "concurrently" in a mixture of $CuCl_2 \cdot xH_2O$, resorcinol, formaldehyde, and an acid scavenger.[80] The high acidity of the $CuCl_2 \cdot xH_2O$ solution catalyzes the polymerization of resorcinol, formaldehyde when heated.[80] The subsequent drying and pyrolysis resulted in

mesoporous carbon impregnated with Cu metal particles that were produced via the carbothermal reduction.

As pointed out previously for such a concurrent gelation/polymerization process,[79] however, it is unclear whether or not both the inorganic and organic components form interpenetrating composite network structures that are continuous "throughout" the solution. This can be problematic when the composite network structures are used further to fabricate a porous TCO material by removing the organic network component. Namely, if the inorganic network component in the composite gel is not sufficiently continuous in the macroscopic scale, the network structure of the material produced from the composite will be continuous only partially and hence suffer from a poor electrical conductivity. Indeed, there has been no report of producing a mesoporous TCO material or mesoporous metal oxide materials in general through this method. Without obliterating the convenience of the one-pot procedure, the method reported herein avoids the potential problem, by adopting a *sequential* gelation/polymerization process where the inorganic gel network structure forms continuously throughout the body of the precursor solution, before upon heating the organic polymerization fully takes place.

3.2 Experimental

3.2.1 Material Synthesis

Multiple samples were prepared by varying three different synthetic parameters, the concentration of the resorcinol, the Sb doping level and the

concentration of the Sn precursor, and the samples were named to reflect these parameters (Table 1). In Table 1, for example, the first character of the sample names represents the resorcinol concentration which can be 0 for the zero amount (0 *M*), L for Low (0.23 *M*), M for Medium (0.45 *M*) and H for High (0.68 *M*); hereafter they are called 0, L, M and H series, respectively. The second character represents the Sb content and can be 0 for no Sb doping, 3 (3 at.%), 6 (6 at.%) and 9 (9 at.%). The third character represents the Sn concentration and can be 3 (0.3 *M*), 4 (0.4 *M*), or 5 (0.5 *M*). Resorcinol (R) forms a polymer gel with formaldehyde (F) and the R/F concentration ratio was fixed at 0.5 for all the samples.

Table 1. Surface areas and pore characteristics of the products. For the sample naming convention, see the Experimental section.

Sample	BET Surface Area (m^2/g)	Pore Volume (cm^3/g)	Average Pore Size[a] (nm)	Porosity[b] (%)
0-6-4	45	0.08	7.2	37
L-0-4	35	0.15	17	51
L-3-4	60	0.16	11	52
L-6-3	66	0.14	8.6	50
L-6-4	89	0.16	7.0	52
L-6-5	77	0.17	8.8	54
L-9-4	91	0.18	7.9	56
M-0-4	36	0.25	28	63
M-3-4	65	0.26	16	65
M-6-3	80	0.28	14	66
M-6-4	81	0.27	14	66
M-6-5	79	0.24	12	63
M-9-4	100	0.28	11	66
H-0-4	36	0.29	33	67
H-6-4	83	0.32	15	69

[a] 4(total pore volume)/(BET surface area)

[b] Based on $Porosity = \frac{PoreVolume}{PoreVolume + \frac{1}{\rho_{ATO}}}$ where ρ_{ATO} =7.02 g/cm^3 is assumed to be the density of non-porous bulk antimony-doped tin oxide.

In a typical synthesis, for the M-3-4 as an example, the sample was prepared by dissolving 0.057 g $SbCl_3$ (Alfa Aesar, 99.9 %) in 5.47 g of absolute ethanol

(Decon) followed by dissolving 2.8 g of $SnCl_4 \cdot 5H_2O$ (Sigma-Aldrich, 99 %). After a complete dissolution, 6.95 g of deionized water was mixed with the precursor solution followed by 1.0 g of resorcinol (Sigma Aldrich, 99 %), and 1.48 g 37 w/w% formaldehyde solution (Sigma-Aldrich, 7 – 8 % methanol as stabilizer) to produce the precursor solution that had a pH of about 2. This mixture was placed in an ice bath and stirred for about 10 minutes. 4.0 g of propylene oxide (Alfa Aesar, 99+ %) was added slowly to the precursor solution while the solution was stirred for less than two minutes. The solution was then removed from the ice bath. While warming up to the room temperature, it became gelated in about one minute to form a translucent light yellow solid gel monolith (pH ~ 5). The gel was then sealed and aged at room temperature for one day, during which the gel shrank by about 20 volume %. The gel became opaque with a red-orange color, which implied some degree of R-F polymerization during the gel aging. The gel was subsequently placed in an oven at 70 °C for five days after which the gel became a hard red-brown monolith with some small cracks.

The monolithic composite gel was then removed and broken up prior to being air-dried for several days. The drying caused the composite materials to shrink noticeably. The particulate were then heated in an ashing furnace for 10 hours at 500 °C to produce a dark blue material that kept the original particulate shapes.

3.2.2 Material Characterization

Nitrogen sorption isotherms were collected on a Micromeritics ASAP 2020 Surface Area and Porosity Analyzer at 77 K. Samples were degassed under

vacuum at 200 °C for 2 hours followed by 300 °C for 6 hours. For surface area calculation, the Brunauer-Emmett-Teller (BET) model was applied to the adsorption branch in the partial pressure range of 0.05 – 0.2 and all samples showed the C value in the range from 60 to 80. For pore size distributions, the Barrett-Joyner-Halenda (BJH) model was applied to the desorption branch with the Halsey thickness curve[82] for non-uniform surfaces and Faass correction[83] to account for multilayer desorption in adsorbed layer thickness estimation. Total pore volume was estimated from the total quantity of gas adsorbed at the data point closest to $P/P_o = 0.98$ on the desorption branch.

Thermogravimetric analysis (TGA) studies were carried out using a Mettler-Toledo TGA/DSC 1 STARe system. Samples were analyzed by heating from 25 to 500 °C at 10 °C/min, holding at 500 °C for 2 hours and finally cooling to room temperature in 30 min. All analyses were carried out under an air flow at 50 ml/min with 70 μL alumina crucibles. Powder X-ray diffraction data were collected using a Siemens D5000 diffractometer with Cu Kα radiation with silicon as an internal standard. Scanning electron microscopy (SEM) studies were carried out with ground samples using an FEI XL-30 Environmental SEM using 30 KeV electrons. For transmission electron microscopy (TEM) studies, samples were prepared by dry-grinding or grinding samples in an absolute ethanol to form a dispersion. For a powder, the TEM samples were carefully dusted onto TEM grids. For a dispersion, a TEM grid was dipped into the dispersion, taken out and dried in air. TEM images were collected using a JEOL 2000FX at an accelerating

voltage of 200 kV. High Resolution TEM images were collected on a JEOL 2010F at an accelerating voltage of 200 kV.

X-ray photoelectron spectroscopic studies (XPS) were carried out using a VG-220IXL spectrometer with a monochromated Al Kα radiation (1486.6 eV, line width 0.8eV). The pressure in the analyzing chamber was kept at the level of 10^{-9} torr while recording the spectra. The spectrometer had the energy resolution of 0.4 eV. All the binding energies were corrected with reference to C(1s) at 285.0 eV. Deconvolution of the spectrum was done using CASA software with the accuracy of 0.2 eV. Shirley background was used for the deconvolution.

The room temperature and temperature-dependent electrical conductivities of the products were measured by using an integrated van der Pauw-Hall system (Quantum Design PPMS). The measurements were carried out on circular pellets pressed from the bulk materials in a van der Pauw four-probe configuration using gold wire and silver paste for making contacts. The pellets for the measurements were prepared by pressing about 0.11 g of powdered samples in a 10 mm die press at 2000, 3000, 4000 and 6000 psi. The optical properties of the products were investigated using a Perkin Elmer Lambda-8 UV-VIS Spectrophotometer with a Reflectance Spectroscopy Accessory to collect diffuse reflectance UV-VIS spectra. The samples were ground for 5 minutes, loaded into a custom sample holder and the spectra were collected at an interval of 4 nm at a scan rate of 120 nm/min with a slit size of 3 nm. Attenuated Total Reflectance (ATR) Fourier Transform Infrared (FT-IR) spectra were collected for the xerogels using a Bruker Vertex 70 FT-IR spectrophotometer with an MCD detector (liquid N_2 cooled, 77

K) with a single reflection ATR accessory (Pike Technologies, MIRacle ATR sampling accessory) and a diamond crystal plate. The spectra range from 850 to 4500 cm^{-1} at a resolution of 1 cm^{-1}.

3.3 Results and Discussion

Figure 15 illustrates the overall synthetic procedure in which the highly mesoporous ATO is produced by creating, drying and calcining inorganic-polymer composite gels that exhibit a 3D interpenetrating network structures. The composite gels are produced by forming a hydrous ATO gel network followed by promoting polymeric R-F gel formation.

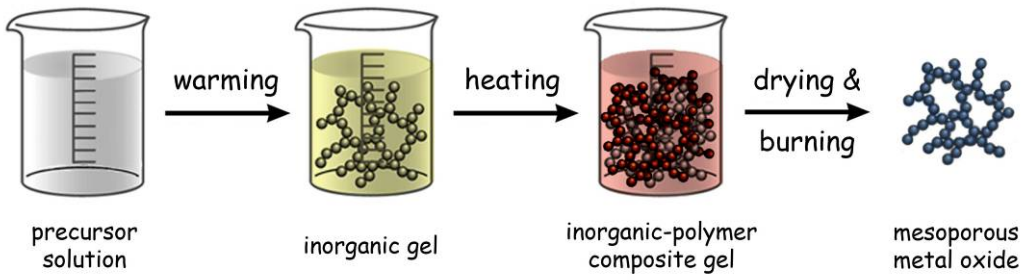

Figure 15. Synthetic scheme of the mesoporous ATO materials.

The synthesis is carried out by first mixing all the reaction precursors in one pot. The solution is acidic (pH ~ 2) because of the hydrolysis of $SbCl_3$ and $SnCl_4 \cdot 5H_2O$ precursors. The precursor solution turns into a translucent light yellow solid gel monolith within about a minute upon warming up after taken out from the ice bath. The gel turns to red-orange after one day at room temperature. At an ambient temperature, the propylene oxide effectively undergoes an addition reaction with the hydrochloric acid to form 1-chloro-2-propanol and a smaller

amount of 2-chloro-1-propanol.[84] The consumption of the acid increases the pH of the solution and induces a uniform formation of an inorganic gel network.[85,86] The yellow color observed for the gel is from the hydrous ATO itself, as was found in a control experiment that the same color was observed even without addition of the R-F polymer precursors. The R-F polymeric gelation can be catalyzed by an acid but the catalysis is effective only at elevated temperatures typically above 60 °C.[87–89] When catalyzed by an acid, the formation of R-F gels is indicated by a distinctive red-brown color which is due to the formation of o-methide quinones as a byproduct.[90] Therefore, the red-orange color of the gel observed after a day may indicate that the R-F polymerization can take place even at room temperature but only slowly in the current experimental condition. This is in contrast to the rapid formation of the hydrous ATO gel that takes place in about a minute.

Upon subsequent heating at 70 °C, the R-F polymerization fully occurred in the hydrous ATO gels to give the unique red-brown color. It is plausible that unreacted metal precursors may catalyze the polymerization, although the pH of the gel is somewhat higher (pH ~ 5) than the typical values used for the effective catalysis of the R-F polymerization.[90] More importantly, it is possible that the inorganic gel network itself may also promote the polymerization, as high valent metal oxides can act as a Lewis acid.[80,81] In order to prove the possibility, a small amount of commercial ATO nanoparticles (Sigma Aldrich, 7 – 11 at.% Sb, 99.5%, <50 nm, surface area ~47 m^2/g) was mixed into an R/F mixture solution and heated at the same condition. The R-F polymerization was apparent from the

gelation of the solution while there was no polymerization when no ATO nanoparticles were added. It is plausible that in the process the pre-formed ATO gel network could play a role in accelerating the R-F polymerization.

The ATO/R-F composite gels were then dried in air to form composite xerogels. Although not shown here, the BET and BJH analysis indicae that the composite xerogels have a low surface area (<10 m^2/g), a negligible pore volume (<0.02 cm^3/g) although pore sizes are still in the mesoscopic range (~5 nm), indicating that the significant porosity of the final products (see below) is not an inherent feature of the composite gels. Their nitrogen sorption isotherms show a very large hysteresis of type H2 which does not close even at relative pressure as low as 0.15. Figure 16 shows the ATR-FT-IR spectrum of an ATO/R-F composite xerogel (M-6-4 composition) along with those of an ATO xerogel (0-6-4 composition) and R-F xerogel for comparison.

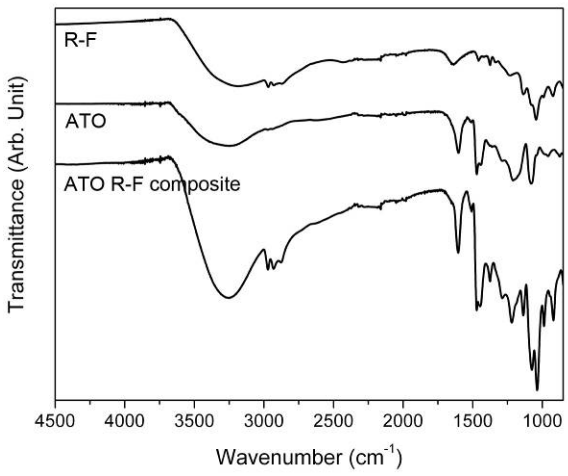

Figure 16. ATR FT-IR spectra for ATO gel, R-F gel and ATO/R-F composite gel after drying.

For the R-F xerogel, the bands around 2900 and 1480 cm^{-1} are associated with the CH_2 stretching and bending vibrations. Meanwhile, the broad band around 3300 cm^{-1} is due to the OH groups of resorcinol for the R-F xerogel, but for the ATO xerogel it probably originates from the hydroxyl groups coordinated to the metal ions. The FT-IR spectrum of the composite xerogel exhibits all the bands of the R-F and ATO xerogels, which is consistent with the compositional nature of the material. Figure 17 shows the thermogravimetic behavior in air of the M-6-4 ATO/R-F composite xerogel together with an R-F xerogel for comparison.

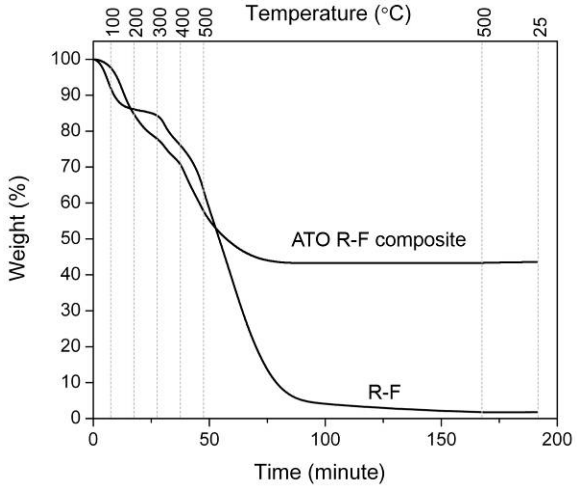

Figure 17. TGA curves for ATO gel and ATO/R-F composite gel after drying.

The initial weight loss of the R-F xerogel below 150 °C is due to the evaporation of residual water and ethanol in the gel material. The further loss at higher temperatures results from the combustion of the organics, which is not complete right when the temperature reaches 500 °C. The material continues to burn at the temperature almost to completeness. While the ATO/R-F composite xerogel shows the similar combustion behavior, the constant weight reached soon at 500 °C indicates that the combustion of the organic component is much faster

than what is found for the R-F xerogel. This is understandable as the R-F network structure itself in the composite gel has a high surface area and hence is in contact with air more efficiently. Furthermore, the TGA results indicate that the dehydration (and thus weight loss) of the ATO gel network is complete below 500 °C while the R-F component continues to burn. Since the dehydration of metal oxide gels is one important cause of pore collapsing, the complete dehydration of ATO at relatively low temperatures does not disfavor the success of the proposed synthetic procedure.

The microscopic structural features of the ATO products were examined by SEM studies on the ground samples (Figure 18).

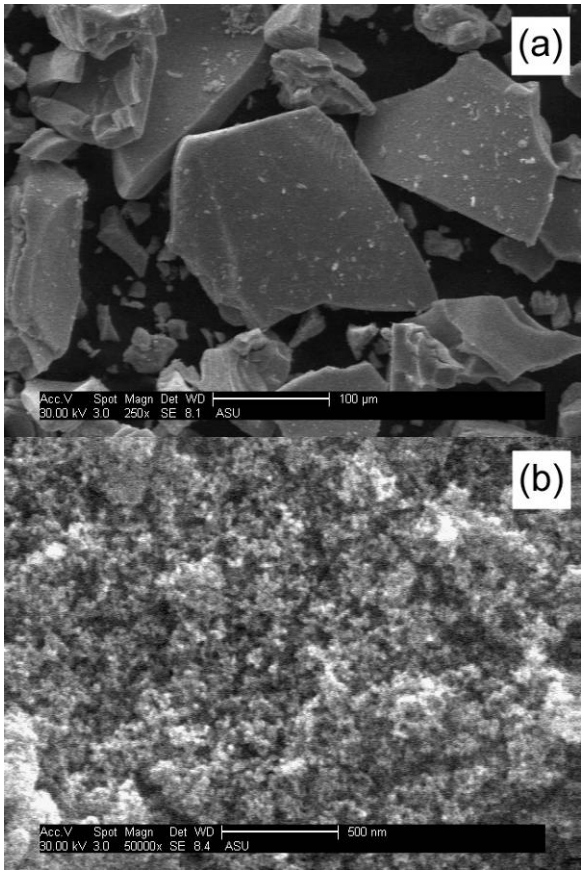

Figure 18. Scanning electron microscope images of the sample L-6-4. The scale bars are 100 μm in (a) and 500 nm in (b).

Figure 18a shows well-defined large particles with dimensions in the order of hundreds of microns. The broken edges of the particles are sharp and their surfaces are flat and smooth, indicating the brittleness of the material. A higher magnification image in Figure 18b reveals that the surface of the particles exhibits a highly porous structure with pores in the meso- or macro-regime. The primary nanoparticles of the prepared material can be seen in the TEM images in Figure 5 and show sizes ranging from 5 to 10 nm.

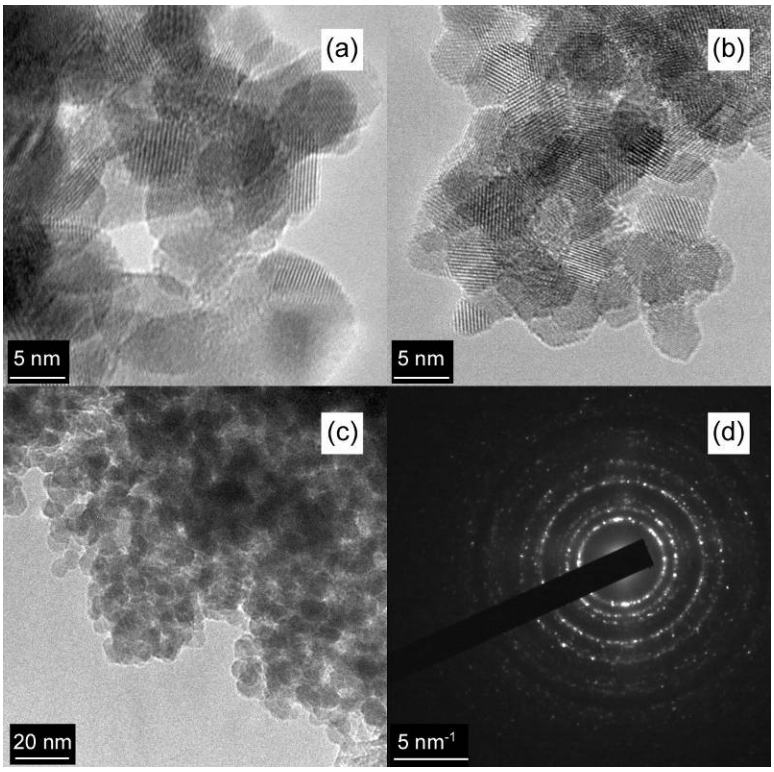

Figure 19. Transmission electron microscope images of (a) M-3-4 (b) M-9-4 and (c) M-6-4 and (d) selected area electron diffraction (SAED) of M-3-4.

The size and appearance of these nanoparticles are similar to those of previously reported ATO nanoparticles from sol-gel routes.[75,91,92] The crystalline nature of the prepared materials is indicated by the lattice fringes apparent in the high magnification images in Figure 19a and b as well as from the selected area electron diffraction (SAED) image in Figure 19d. Powder X-ray diffraction (PXRD) patterns shown in Figure 20 confirm the crystallinity of the prepared materials, although the Bragg peaks are relatively broad.

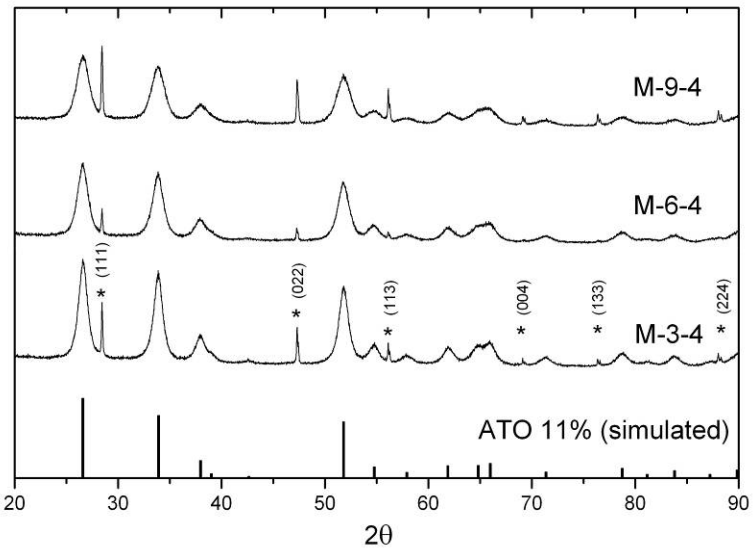

Figure 20. Powder XRD patterns of the M series with 0.4 *M* Sn precursor concentration with the simulated pattern of an ATO (11 at.% Sb, ICSD 41530). Silicon standard peaks are marked with stars.

The patterns are for three Sb-doped samples of the M series with the 0.4 *M* Sn precursor concentration (M-3-4, M-6-4 and M-9-4). The series was chosen because their surface areas and porosity are the maximum among the series. In addition, they show a clear trend in surface areas, pore sizes and pore volume. The other series of samples with lower and higher R-F contents (the L and H series) do not exhibit such remarkable trends.

All the products exhibit a cassiterite structure, in agreement with the literature data for ATO (11 at.% Sb, ICSD No. 41530). Silicon was also added to the PXRD samples (diffraction peaks indicated with stars) as an X-ray diffraction standard. No noticeable peak shifts were observed except a slight shift of the (110) peak to the higher angles at around 26°, which is likely due to the relatively low doping levels.[75] However, it shows a trend of increasing peak width with the Sb doping concentration, which indicates decreasing crystallite size with

increasing Sb content. The particle sizes estimated from Scherrer's formula were 10, 8.0 and 6.6 nm for M-3-4, M-6-4, and M-9-4 respectively. These are consistent with the literature values with Sb doping levels below 15 at.%.[91] The trend in the particles sizes of those three samples is reflected in the BET surface area of the products, as shown in Table 1. The BET surface area gradually decreases from 100 (M-9-4) to 65 (M-3-4) and to the lowest value of 36 m^2/g for the undoped product (M-0-4).

Figure 21 shows the N_2-sorption isotherms of the M series of samples M-0-4, M-3-4, M-6-4, and M-9-4.

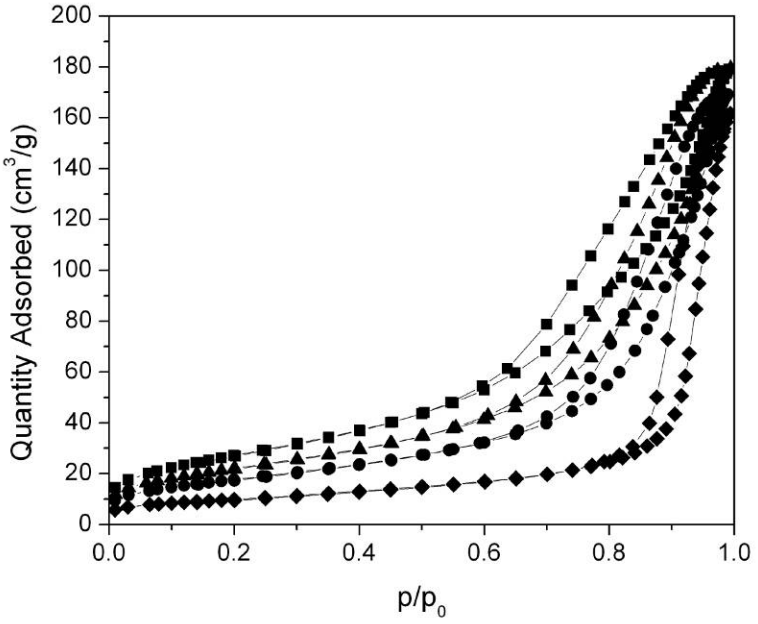

Figure 21. N_2-sorption isotherms for M-0-4 (◆), M-3-4 (●), M-6-4 (▲), M-9-4 (■).

The presence of the hysteresis loops indicates the existence of mesopores in the products. The hysteresis loops shift to lower pressures with increasing Sb content,

which indicates a decrease in pore size. This trend is seen more directly in the BJH pore size distribution plots in Figure 22.

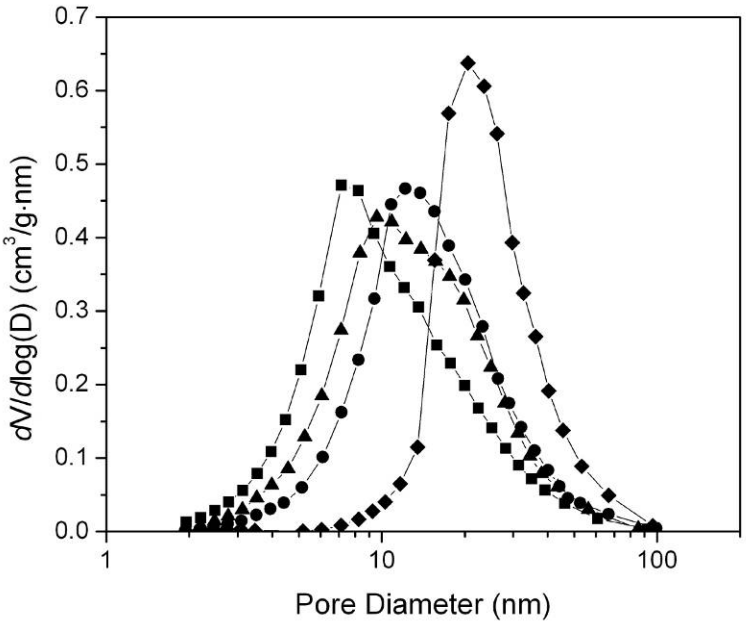

Figure 22. BJH pore size distributions for M-0-4 (◆), M-3-4 (●), M-6-4 (▲), M-9-4 (■).

The average pore size decreases from 16 to 11 nm as the Sb content increases in the series (Table 1). The doped products (M-3-4, M-6-4, and M-9-4) exhibit broad, but distinct pore distribution curves (Figure 22). The pore size distributions shift to larger pore diameters with decreasing Sb content. Ultimately, the sample M-0-4, an undoped SnO_2 material, shows a broad pore size distribution with the largest pore sizes centered around 22 nm. It has been indicated in the literature that the primary particles grow larger during the synthesis in the absence of Sb metal ions.[91] This was also the case in the described experiments in that the average particle size of M-0-4 is 13 nm from the PXRD pattern (not shown). The relatively narrow pore distribution found for M-

0-4 may be due to the particle growth at the expense of relatively small pores. This results in the observed increase in average pore size with the decrease in the Sb content. However, this sacrificial growth of the pores affects the total pore volume only slightly. The samples M-0-4, M-3-4, M-6-4 and M-9-4 show total pore volumes of 0.25, 0.26, 0.27 and 0.28 cm^3/g respectively.

It is found that the pore volume is more effectively controlled by changing the R-F polymer precursor content. For example, in the series of the samples 0-6-4, L-6-4, M-6-4 and H-6-4, the pore volume increases drastically from 0.08 to 0.32 cm^3/g (Table 1), which is obvious also from the increasing absorbed gas amount in the N_2-sorption isotherms (Figure 23). Especially, the sample 0-6-4, prepared without the R-F precursors, has a significantly lower pore volume than the ones with them.

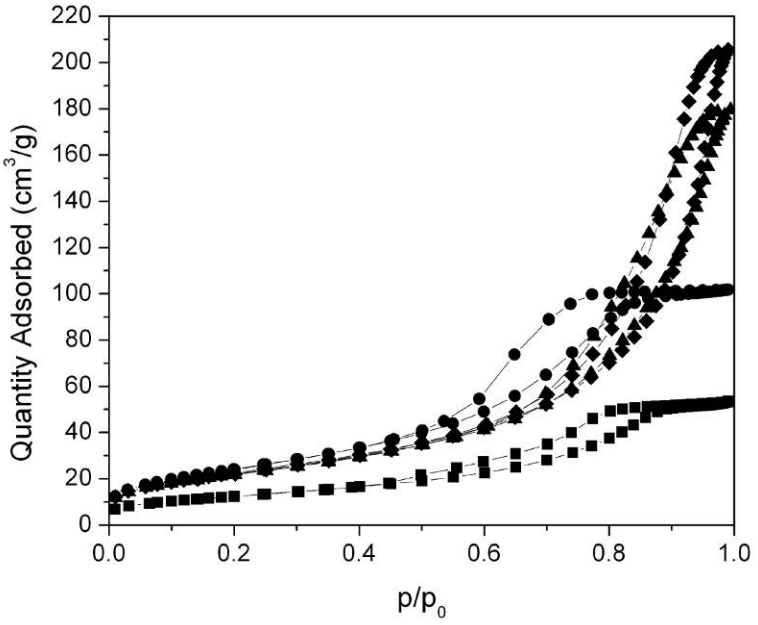

Figure 23. N_2-sorption isotherms for 0-6-4 (■), L-6-4 (●), M-6-4 (▲), H-6-4 (◆).

This is understandable if the role of the R-F polymer network as a hard template is considered. After forming the interpenetrating hydrous ATO and R-F polymer network structure, the composite materials are subjected to drying and calcination during which both gel shrinkage and pore collapsing take place. As the composite gel dries out, both the ATO and R-F networks shrink due to the capillary force exerted on the pore wall. In comparison to an ATO gel without the interpenetrating R-F network component, the shrinkage and consequent pore collapsing is expected to be less severe in the composite gel because the R-F polymer network does not evaporate and remains inside the ATO pore network as a template. Furthermore, those materials with higher polymer contents would be expected to be more resistant to the shrinkage and pore collapse due to the larger physical volume of the R-F polymer present in the composite gel.

The pore volume increase with increasing R-F polymer content is accompanied by increasing pore sizes (Table 1). In the BJH pore distribution (Figure 24), sample 0-6-4 has essentially all of the pore volume coming from the pores between 2 and 20 nm in size. By including a small amount of polymer as for the sample L-6-4, however, the total pore volume from the same 2 – 20 nm range is increased markedly. Increasing the polymer content further results in significant pore volume contributions from large mesopores and also from small macropores in the range of 50 – 100 nm which are not present in the low polymer content composites.

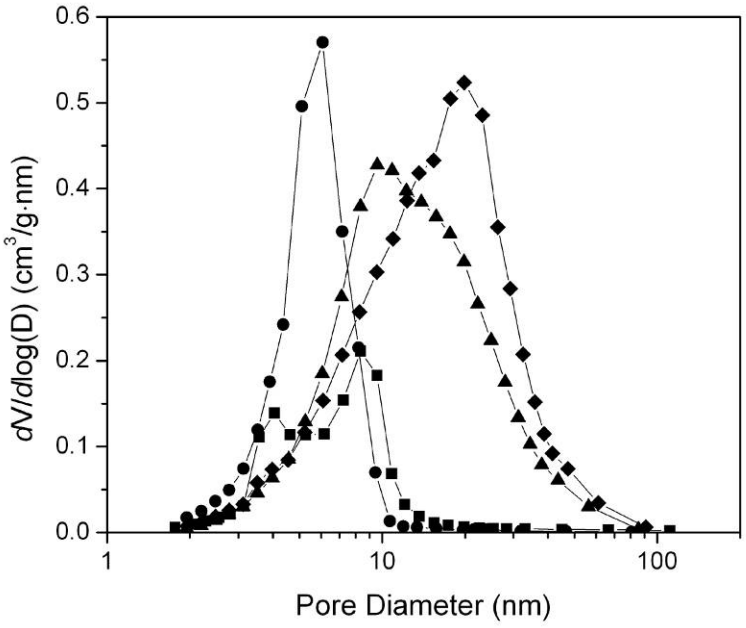

Figure 24. BJH pore size distributions for 0-6-4 (■), L-6-4 (●), M-6-4 (▲), H-6-4 (◆).

This control of pore sizes is critically important when the product materials are to be used in sorption of large molecules such as proteins and DNA nanostructures. In separate studies where the mesoporous ATO was prepared in thin films (~ 400 nm thick), for example, it is demonstrated that these porous materials possess the capability of hosting the tetrahedral DNA nanocage (20 base pairs on each helical edge, corresponding to ~ 6.8 nm per side) with high affinity but only for the large pore product.[93] The mesoporous ATO films with an average pore size of 14 nm (M-6-4) absorbed the DNA nanocages strongly, while the one with a 7 nm average pore size (L-6-4) did not show any appreciable absorption.[93]

The XPS of Sn(3d) core level region for the sample M-6-4 is shown in Figure 25a. Binding energies of the Sn($3d_{5/2}$) and Sn($3d_{3/2}$) appear at 487.0 eV and 495.5 eV, respectively. The binding energy values confirm that the Sn atom is in its 4+

oxidation state in the mesoporous ATO products.[94] Similarly, the XPS of the Sb(3d) core level region was also analyzed (Figure 25b). Because of the very low binding energy difference between O(1s) and Sb($3d_{5/2}$), only Sb($3d_{3/2}$) region is shown. The Sb($3d_{3/2}$) peak is asymmetric and thus is deconvoluted based on the fact that Sb^{5+} and Sb^{3+} ions can coexist in ATO.[94–96] The deconvoluted Sb($3d_{3/2}$) spectrum clearly shows the presence of Sb^{5+} (90%) and Sb^{3+}(10%). Therefore, the mesoporous ATO can be considered as an n-type doped conductor.

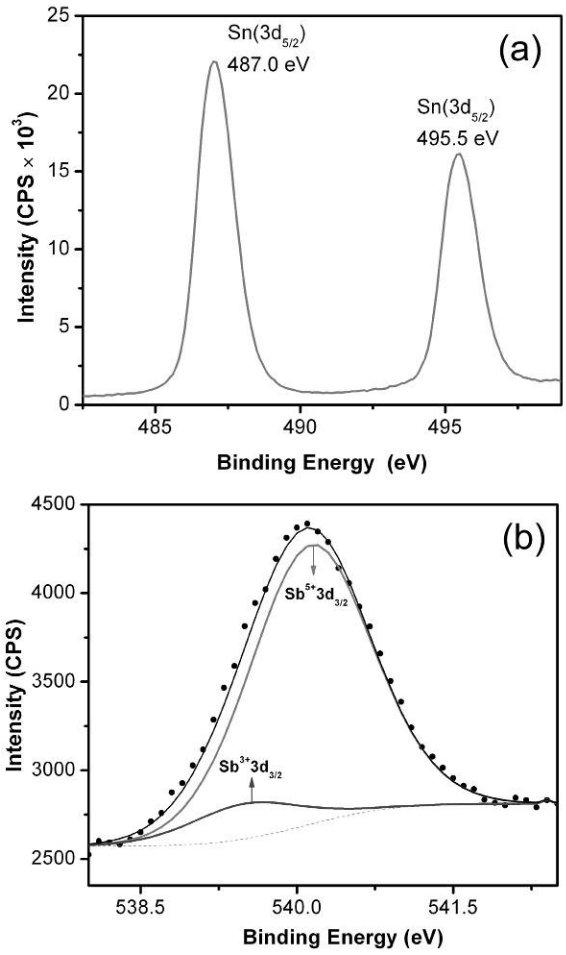

Figure 25. XPS of the core level regions of (a) Sn(3d) and (b) Sb(3d) in as prepared M-6-4 sample. The deconvoluted peaks of Sb^{5+}($3d_{3/2}$) and Sb^{3+}($3d_{3/2}$) with binding energy peaks at 540.1 eV and 539.2 eV, respectively, are given in grey lines. The broken line is the background.

Resistivity measurements were carried out on pellets pressed from the ground bulk materials in a four-probe van der Pauw configuration. Two series of pellets were prepared with either varying the Sb content or pelletizing pressure for the M series samples. Table 2 shows the room temperature resistivity values and the surface/pore characteristics as a function of the pressure applied to form the pellets.

Table 2. Electrical resistivity at room temperature and the pore characteristics of selected pellet samples prepared under various pressures.

Sample	Pressure (*psi*)	Resistivity (*Ω-cm*)	BET Surface Area (m^2/g)	Pore Volume (cm^3/g)	Average Pore Size[a] (*nm*)
M-0-4	2000	8.03	46	0.216	19
M-3-4	2000	0.250	63	0.233	15
M-6-4	2000	0.540	77	0.241	13
M-9-4	2000	0.290	92	0.243	11
M-6-4	14.7	–[b]	81	0.274	14
M-6-4	3000	0.140	74	0.185	10
M-6-4	4000	0.140	78	0.177	9.1
M-6-4	6000	–[b]	77	0.152	8.0

[a] 4(total pore volume)/(BET surface area)
[b] The sample did not form a whole pellet for resistivity measurement.

The resistivities of the doped products are in the range of 0.14 to 0.54 Ω-cm which is far higher than the values obtained for dense ATO films (down to 1×10^{-3} Ω-cm). However, the values are still lower than the lowest resistivity (*ca.* 1.3 Ω-cm) reported for a mesoporous ATO material, despite that the material had smaller pore sizes (< 10 nm) and lower porosities (~ 50%).[75] As far as the effect of the pressure applied during the pellet preparation is concerned, the resistivity is

observed to decrease with increasing applied pressure for the same composition sample (M-6-4 in Table 2). At the same time, the pore volume and the porosity decrease upon increasing pressure, while the surface area is less dependent of the applied pressure (Figure 26).

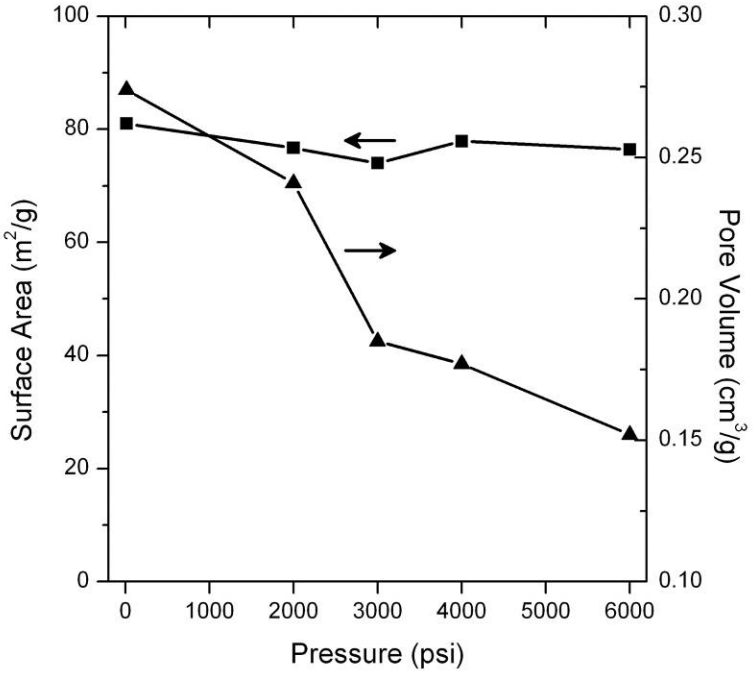

Figure 26. BET surface area and total pore volume of M-6-4 pellets pressed at various pressures.

Reducing porosity and increasing interfacial area between ATO nanoparticles by compaction should increase the number of pathways for charge transport, resulting in a lower resistivity.

The electrical properties of the prepared samples were further investigated by collecting temperature-dependent conductivity data for the M-6-4 pressed at 2000 psi from 90 to 280 K. The variation of the logarithm of conductivity as a function of reciprocal temperature is shown in Figure 27.

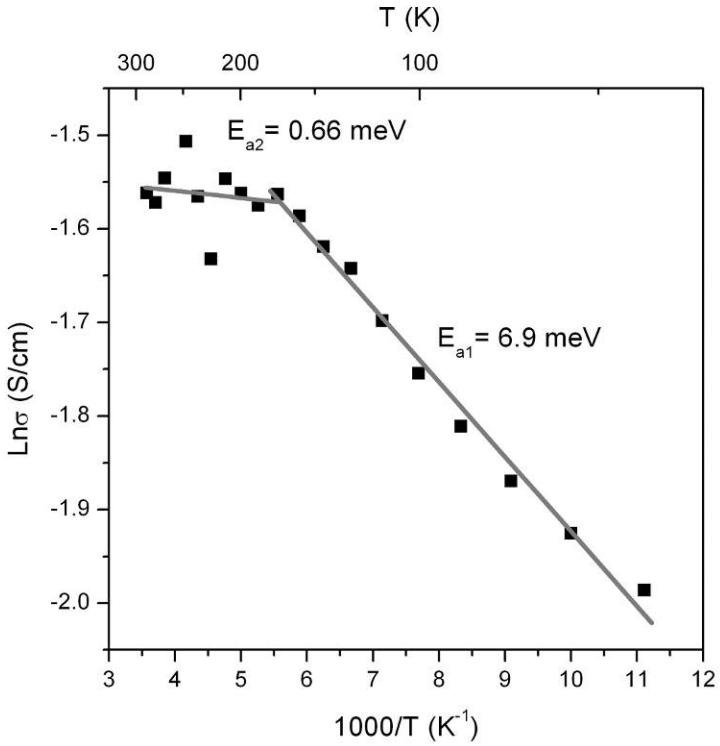

Figure 27. Temperature-dependent conductivity of M-6-4 pellet pressed at 2000 psi.

Two regimes in which the logarithmic values change more or less linearly with different slopes are observed. Activation energies calculated from the two slopes are found to be 6.9 meV (< 180 K) and 0.6 meV (> 180 K). It has been reported that the energy of the donor state of ATO is about 35 meV below the conduction band.[97{Citation}] The value is much larger than the two activation energy values estimated for the M-6-4 sample. It is likely that other donor states exist closer to the conduction band and provide the observed relatively high conductivity.

The optical properties of the prepared materials were investigated using UV-Vis diffuse reflectance spectroscopy. A Kubelka-Munk transform was applied to the diffuse reflectance data to provide a better interpretation of the weakly absorbing samples (Figure 28).

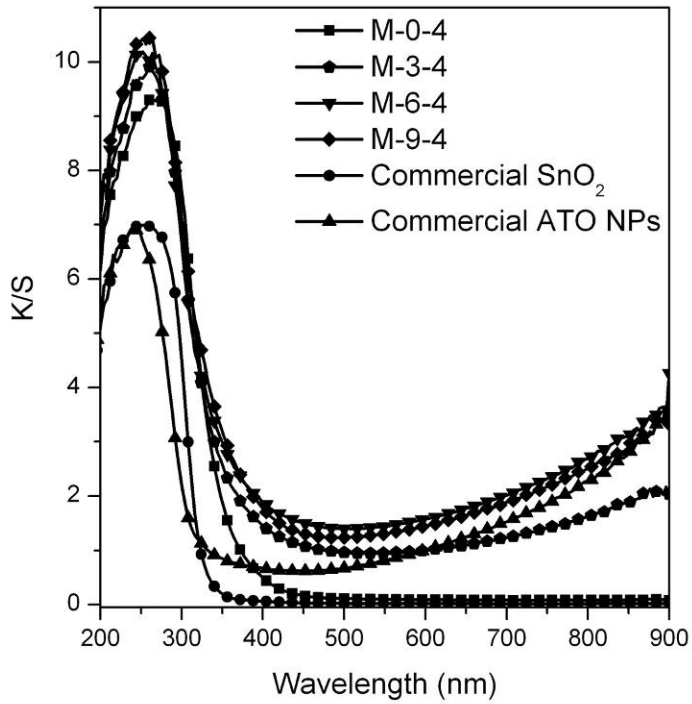

Figure 28. Kubelka-Munk transform of UV-Vis diffuse reflectance spectra for selected samples.

Two commercial powders of non-porous SnO_2 (Alfa Aesar, 99.9%, <10 μm) and the ATO nanoparticles were also characterized for comparison. Both commercial SnO_2 powder and the sample M-0-4 (an undoped product) show the onset of absorption at a wavelength of about 300 nm, showing the inherent absorption of SnO_2. All the ATO materials exhibit a gradual increase in light absorption over 300 nm. The absorption in the visible region is responsible for the blue color of the ATO products and is due to the Sb doping.[98,99]

3.4 Conclusion

It has been demonstrated herein that a facile one-pot process can produce highly mesoporous ATO materials with controllable pore sizes and porosity through

formation, drying and calcination of interpenetrating hydrous ATO and resorcinol-formaldehyde composite gel networks. In one respect, the new process can be considered as a convenient double-nanocasting method. The firstly formed hydrous ATO gel network acts as a nanocast for the secondly forming polymer gel network. In turn, the polymer gel network plays the role of a nanocast for the ATO network during drying and calcination of the composite gel. The physical presence of the polymer component inside the inorganic gel network alleviates the extent of pore collapsing by buttressing the inorganic structure during its drying, dehydration and crystallization. The 3D interconnected textural mesopores in the resulting ATO material can be ideal for efficient flow and adsorption of molecules in the material. The well-sintered/connected ATO nanoparticles in the structure gives a high electrical conductivity. Further applications of the process may provide other interesting mesoporous metal oxide materials in various forms including thin films which may provide advances for fields such as electrooptical devices,[37] solar energy generation,[73] and chemical sensing[100] where the high surface area of conducting electrodes may have an advantage despite the resulting relatively low conductivity.

CHAPTER 4

MESOPOROUS CARBON

4.1 Introduction

The high surface area and electrical conductivity of many synthesized carbon materials have been implemented in electrochemical devices like batteries,[12] fuel cells,[13] and capacitive deionization technologies.[101] High surface area carbons also have particular application in electrochemical double layer capacitors (EDLCs) due to the proportionality of the total capacity of a device and the specific surface area.[102,103] Many high surface area carbons owe their exceptional specific surface area to the presence of micropores and in many preparations, carbons are treated specially to enhance this characteristic.[104,105] However, a direct correlation between measured surface areas and measured capacitances is not seen in microporous carbon samples which can be due to the inability of micropores to be wetted by electrolyte, and thus not accessible for double layer capacitance.[70,106] Additionally, in the case of a wetted micropore, it is not clear if true double layer formation can even occur in these restrictive confines. At high electrolyte concentration, double-layer capacitance is mostly from the compact Helmholtz layer[68] and can extend to about 1 nm into the electrolyte solution[69]. Micropores have pore widths less than 2 nm which could frustrate the formation of double-layers on opposing pore walls. Gogotsi et al. have reported a special mechanism for infiltration of micropores of ions stripped of their solvation shell that can contribute to a capacitive effect, but the reported phenomena still need further characterization.[107,108] It is generally recognized that when a micropore is

wetted with electrolyte, slow charge/discharge rates (or potential sweep rates) must be used to allow the signal to penetrate into the pore.[109] This is due to a change in potential relative to the depth within a pore. There is a progressive increase in electrolytic resistance down a pore from its opening leading to a so-called "penetration depth".[110,111] It is generally recognized that the inclusion of mesoporosity in electrochemical devices employing double-layer formation is highly advantageous[102], especially when the mobility enhancement of ions in larger pores is considered.[70]

Existing methods for preparing mesoporous electrodes include inherently porous materials like carbon aerogel[102,112] as well as carbons with pore volumes generated with removable templates.[45,113] Carbon aerogel preparations produce high specific surface area solids with continuous porosity but suffer from high energy and material consumption. Many templating techniques require the synthesis of the template prior to the preparation of the desired porous material and producing well controlled continuous porosity on large length scale is challenging. Here a method is present that demonstrates the use of an *in-situ* formed inorganic gel template that catalyzes the polymerization of a carbon precursor polymer in a one-pot preparation. The formed interpenetrating porous networks allow for energy efficient ambient drying methods to be employed without catastrophic pore collapse due to capillary forces. Additionally, the inorganic gel is a continuous solid structure, so when used as a template, the pore space left behind upon removal is assured to be continuous throughout the body of the remaining carbon solid.

4.2 Experimental

4.2.1 Mesoporous Carbon preparation

An interpenetrating gel network of alumina gel and RF polymer was prepared in bulk by first using epoxide driven gelation for the inorganic component most recently popularized by Gash et al.[114,115] First, 142 g of $AlCl_3 \cdot 6H_2O$ was dissolved in 1.2 L of 50 % aqueous ethanol in a large jar. Then 20 g of resorcinol was added and stirred until dissolution was complete. 30 g of formaldehyde solution (37 % by weight) was added to the solution with stirring. This precursor solution was then constantly stirred while propylene oxide was added in approximately 100 ml aliquots every 4 minutes until a total of 412 ml was added. This solution was stirred for about 20 minutes, covered with a lid, and then left to gel undisturbed. The solution gelled into a clear colorless gel in less than 1 hour. The gel was left at room temperature for about 18 hours and then placed in an oven at 70 °C for 4 days to promote the polymerization of the RF precursors. The dark red gel was then removed from the oven, chopped into pieces less than 1 cm in dimension, and air dried under a fume hood for about 2 weeks. The dried composite xerogels were pyrolyzed in a tube furnace purged with argon. The furnace was ramped at a rate of 6 °C per minute to 1000 °C and held for 3 hours, all under flowing argon gas. The resulting metal oxide carbon composites (MOCCs) were then treated to etch the alumina component. The MOCCs were placed in a 1 L round-bottom flask with a water-cooled reflux condenser and refluxed in 425 ml of 19 % hydrochloric acid for 5 hours. The resulting mesoporous carbon was then separated from the filtrate and rinsed with water

using a vacuum filter. The carbon was washed with water until the pH of the filtrate was neutral, then placed in an oven at 110 °C for 24 hours to dry.

4.2.2 Electrode preparation

The mesoporous carbon was ball milled for 45 minutes using steel balls to produce a fine powder. The mesoporous carbon was mixed with acetylene black and Nafion 117 solution into a paste that was spread onto pre-weighed strips of carbon fiber tissue (0.5 oz/yd^2, The Composite Store, Tehachapi, CA). The final solids weight ratio of mesoporous carbon : acetylene black: Nafion was 85:10:5. These electrodes were pressed between steel plates at 4000 psi and then dried in an oven at 110 °C for 1 hour.

4.2.3 Material Characterization

Nitrogen sorption isotherms were collected on a Micromeritics ASAP 2020 Surface Area and Porosity Analyzer at 77 K. Samples were degassed under vacuum at 200 °C for 8 hours. For surface area calculation, the Brunauer-Emmett-Teller (BET) model was applied to the adsorption branch in the partial pressure range of 0.05 – 0.2 and all carbon samples showed BET C values near 100. For pore size distributions, the Barrett-Joyner-Halenda (BJH) model was applied to the desorption branch with the Carbon Black STSA thickness equation and Faass correction[83] to account for multilayer desorption in adsorbed layer thickness estimation. Total pore volume was estimated from the total quantity of gas adsorbed at the data point closest to P/Po = 0.98 on the desorption branch.

Thermogravimetric analysis (TGA) studies were carried out using a Mettler-Toledo TGA/DSC 1 STARe system. Samples were analyzed by heating from 25 to 700 °C at 10 °C/min, holding at 700 °C for 30 minutes and finally cooling to room temperature in 30 min. All analyses were carried out under an air flow at 50 ml/min with 70 μL alumina crucibles.

Powder X-ray diffraction data were collected using a Siemens D5000 diffractometer with Cu Kα radiation. Scanning electron microscopy (SEM) studies were carried out with ground samples using an FEI XL-30 Environmental SEM using 10 keV electrons. For transmission electron microscopy (TEM) studies, ground samples were carefully dusted onto TEM grids. TEM images were collected on a JEOL 2010F at an accelerating voltage of 200 kV.

Electrodes were prepared to contain approximately 10 mg of active material. Electrochemical measurements were performed with a CHI760C electrochemical analyzer in 3 M H_2SO_4 and in 200 mM $TEAPF_6$ in acetonitrile in a three electrode cell. Platinum mesh was used as a counter electrode and Ag/AgCl was used for the reference electrode. In the case of acid electrolyte, electrodes were vacuum infiltrated prior to measurement.

Raman data were collected using a custom built Raman spectrometer in a 180 ° geometry. The sample was excited using a 100 mW Compass 532 nm laser. The laser power was controlled using neutral density filters and reduced to a power of 5 mW at the sample surface. The laser was focused onto the sample using a 50X super long working distance Mitutoyo objective with a numerical aperture of 0.42. The signal was discriminated from the laser excitation using a

Kaiser laser band pass filter followed by a Semrock edge filter. The data were collected using an Acton 300i spectrograph and a back thinned Princeton Instruments liquid nitrogen cooled CCD detector.

4.3 Results and Discussion

The porous materials prepared were analyzed at several stages during their preparation. Nitrogen-sorption isotherms were collected and pore size distributions were calculated for the MOCCs prior to the extraction step and can be compared to the same of the etched carbon sample and the ball-milled carbon sample in Figure 29.

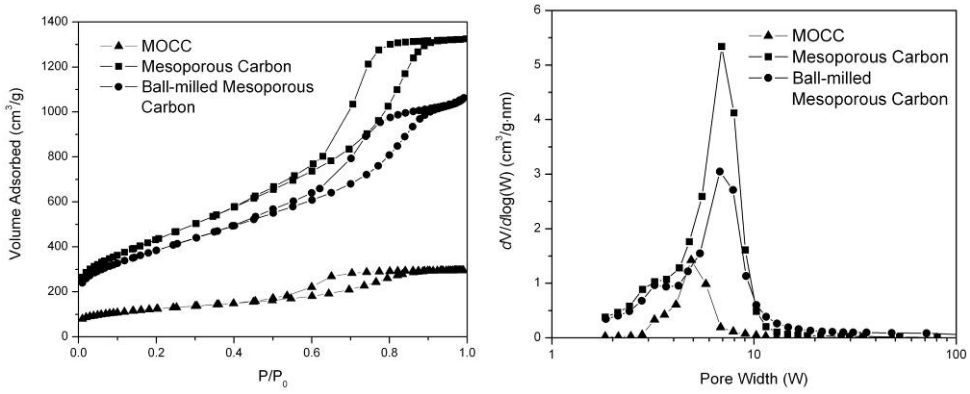

Figure 29. Nitrogen isotherms and BJH pore size distribution plots of the MOCC composite, mesoporous carbon, and the ball-milled mesoporous carbon.

All materials show the presence of a hysteresis loop indicating mesoporosity. The MOCC material shows the lowest adsorption capacity because both inorganic and organic networks remain within the porous structure, but it is still highly porous. The porous carbon produced after etching the alumina component out of the MOCC shows the highest adsorption capacity and the ball-milled carbon at an

intermediate amount. The pore size distributions show that the MOCC has smaller pore sizes present, most likely because the large mesopore volume seen in the carbon samples is still filled with the inorganic template. Upon removal of the oxide template, there is a large increase in pore volume from pores between 6-10 nm seen in the mesoporous carbon sample and the ball-milled carbon sample. Additionally there is a reduction in pore volume following the ball milling step. The pore size distributions in Figure 29 show that both carbon samples have the approximately the same pore distributions, but the ball-milled samples show a large reduction in mesopore volume between 4 and 8 nm. Under close inspection, the pore size distribution for the ball-milled carbon shows a slight increase of large mesopore volume between 10 and 50 nm relative to the un-milled carbon. There is also a suggestion of the generation of macropores caused by the ball milling step due to the slight upturn in the nitrogen isotherm for the ball-milled carbon at P/P_o close to 1. This occurs in the presence of macropores that cannot be completely filled by capillary condensation.[67] The TEM images in Figure 30 show the origins of the mesoporosity in the porous carbon prior to ball milling.

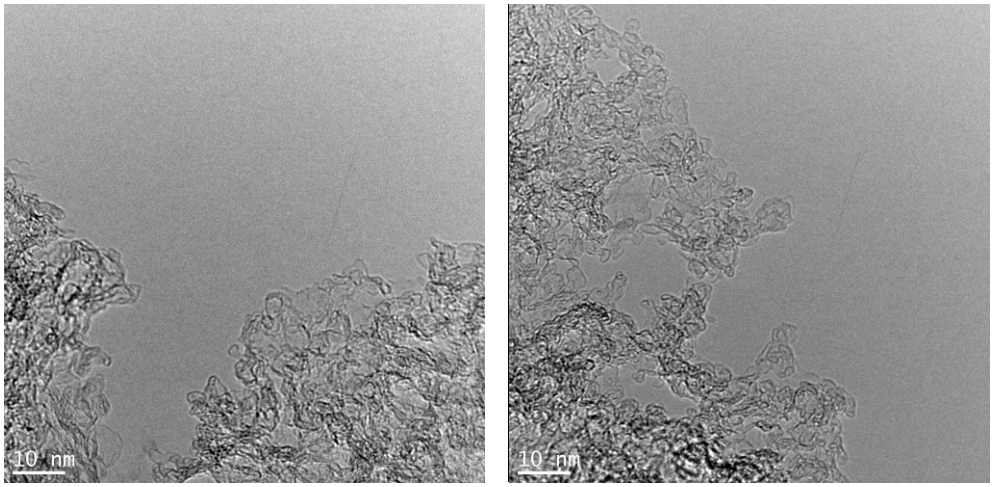

Figure 30. TEM images of mesoporous carbon.

Very thin shells of carbon can be seen extending in many directions. There is large volume of pore space present within the confine of these tenuous shells as well as the regions between the different carbon shells that lie well within the mesopore range of 2 to 50 nm. This complicated architecture is a consequence of the synthesis technique wherein an inorganic gel network was first formed and the surface of this inorganic gel catalyzes the polymerization of the organic polymer gel network. This synthetic method was described in Chapter 3 of this thesis, but in the present method, the organic component is preserved and the inorganic component is removed. Upon inorganic network removal, the thin carbon walls are left behind in a manner not unlike the arts and crafts technique of papier-mâché. The SEM image in Figure 31 shows that this continuous network extends well into the macroscale.

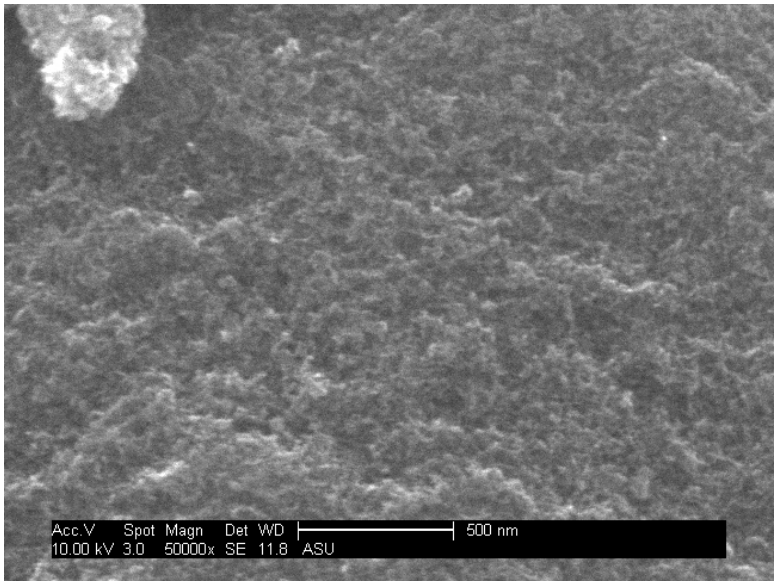

Figure 31. SEM image of a large piece of mesoporous carbon.

The surface areas pore volumes and average pore sizes were calculated from the nitrogen sorption isotherms and are shown in Table 3.

Table 3. Surface area and pore characteristics of mesoporous carbon and ball-milled mesoporous carbon

Sample	BET surface area[a] (m^2/g)	Pore Volume[b] (cm^3/g)	Average Pore Size[c] (nm)	Porosity[d] (%)
MOCC	442.2	0.456	4.13	-
Carbon	1561	2.05	5.24	81.5
Ball-milled Carbon	1380	1.63	4.72	77.8

[a] Pressure range P/P_o = 0.05-0.2
[b] Single point desorption nearest P/P_o = 0.98
[c] 4V/A (BET)
[d] $porosity = \left(\frac{PoreVolume}{PoreVolume + \frac{1}{\rho}} \right)$ and $\rho = 2.15$ g/cm^3

There is a drastic increase in specific surface area and pore volume upon removal of the inorganic template. Also noted is the increase in average pore size due to the formation of mesopores in the 6-10 nm range as previously noted in the

analysis of the BJH pore size distribution. Ball milling the carbon sample appears to have a destructive effect on the porous structure, reducing the total pore volume and average pore size. The ball milling process is probably destroying the thin mesopore shells as well as compacting the inter-particle spaces in the open templated structure.

The alumina removal by dissolution in hydrochloric acid was shown to be complete through thermogravimetric analysis. The sample was shown to leave essentially no inorganic mass after combustion in air as seen in Figure 32.

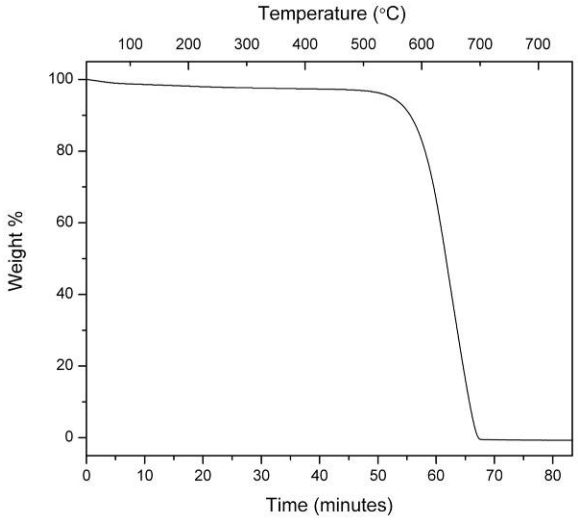

Figure 32. Thermogravimetric Analysis of mesoporous carbon after alumina removal.

The dissolution of alumina in excess hydrochloric acid generates an acidic solution of aluminum chloride.[116] This particular aspect is also indicative of the recyclability of the alumina template. The gel precursor solution consists of an acidic solution of aluminum chloride salt and could be regenerated from the etching solution produced during template removal without large modification.

The porosity of the prepared materials has been confirmed, but for the material to exhibit conductivity, some crystalline order must be present. Powder X-ray diffraction patterns were collected for both the porous carbon and the ball-milled carbon and compared to a calculated graphite pattern as shown in Figure 33.

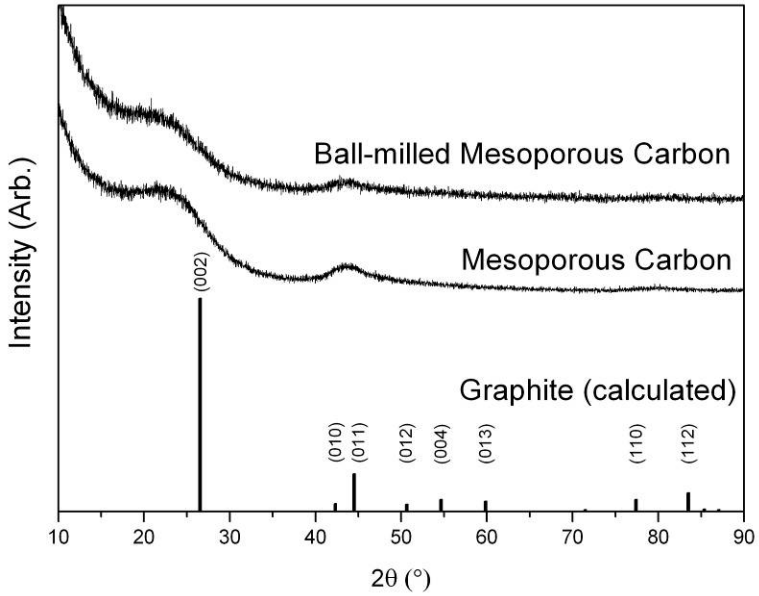

Figure 33. Powder X-ray diffraction of mesoporous carbon and ball-milled carbon as compared to a calculated graphite pattern.

The (002) graphite peak is at approximately 26.5 ° and in both carbons, a very diffuse peak at 2θ less than 30 ° can be observed. This apparent peak shift is not likely due to an increase in the d-spacing in the crystallographic c-direction which would correspond to the graphite layers being spaced further apart. The diffuse peak appears to be constructively interfered with by an instrumental background signal with a decreasing intensity from 10 to about 40 °. Nevertheless, the peak is broad indicating very small crystallite thicknesses in the [002] direction, which means that there are few graphite layers making up the crystallites. Between 40

and 50 °, there is a broad peak that appears to be a combination of the (010) and (001) peaks shown in the graphite pattern. The presence of these peaks indicate that the graphite layers are not randomly rotated relative to one another as in turbostratic graphite[60], but there exists a regular ABAB stacking as each of the <010> and <001> planes consist of atoms in alternating planes. Additionally, the mesoporous carbon also shows a diffuse hump near 80 ° that is near the graphite (110) and (112) peaks which also indicate regular stacking of graphite sheets. These peaks are less pronounced in the ball-milled carbon and could suggest a disruption in the ABAB stacking of hexagonal graphite which has been reported during the grinding of graphite materials.[59] Overall, this data indicates that there are graphite-like crystallites consisting of few layers, but still good intra- and inter-layer order. This seems reasonable when viewing the TEM images in Figure 30, and seeing the very thin solid walls that exist.

The graphitic nature of the prepared carbons was also investigated using Raman spectroscopy. Figure 34 shows the collected Raman spectra for the mesoporous carbon and the ball-milled porous carbon. Peaks near 1600 cm^{-1} and 1350 cm^{-1} are observed, and are the so called G and D peaks respectively.

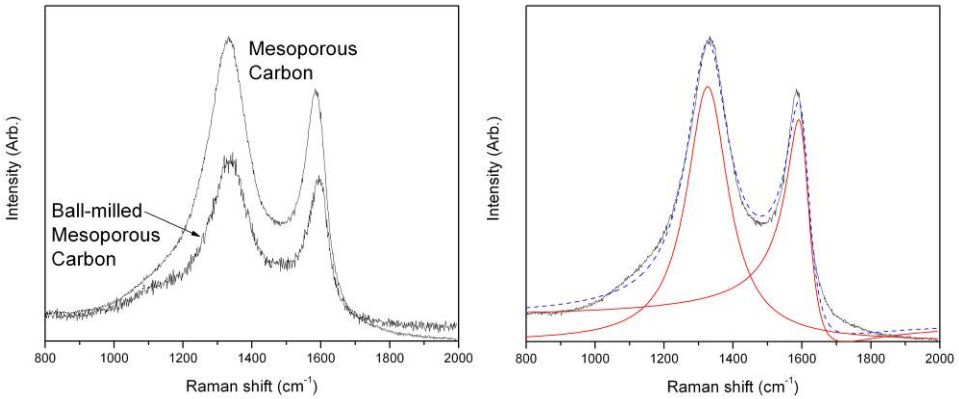

Figure 34. Raman spectra of mesoporous carbon and mesoporous ball-milled carbon. Also shown is the fitted lineshape (dashed line) of mesoporous carbon for determining relative peak intensities.

Tuinstra and Koenig observed proportionality between the intensity ratio of the D and G peaks to the inverse of the crystallite size (L_a) determined by X-ray diffraction.[64]

$$\frac{I(D)}{I(G)} = \frac{C(\lambda)}{L_a} \qquad (1)$$

As shown in equation 1, the intensities of the D and G bands are dependent on the wavelength of the investigating laser, so Cançado et al. modified the equation to account for the use of different laser energies.[117] However, this equation was derived from the ratios of integrated peak areas, which at large crystallite sizes is inconsequential. At small crystallite sizes, the D band width changes due to parameters other than crystallite size, and thus peak intensity ratios should be calculated.[118] The work of Cançado et al. still shows that with decreasing laser energy the intensity of the D band increases. This means that equation 1 can be used as a lower bound for crystallite size when the laser energy is less than the 488 nm laser used by Tuinstra and Koenig for the derivation of this equation. The

peak intensites were determined following the suggestions of Ferrari and Robertson by fitting a Breit-Wigner-Fano line to the G peak and a Lorentzian line to the D peak as shown in Figure 34.[119] Using equation 1 with C(λ) = 4.4 nm and the measured I(D)/I(G) of 1.23 collected using a 532 nm laser for the mesoporous carbon generates a lower bound for crystallite size of about 3.6 nm. Similarly, a crystallite size of about 3.5 nm is calculated for the ball-milled carbon. This crystallite size is in the crystallographic a-direction, or in-plane for the graphite sheets. Given the scale of the thin carbon walls observed in the TEM images, it seems that the graphite-like crystallites would have to be oriented tangent to the pore surfaces to exhibit the crystallite diameters calculated from the Raman data.

The prepared carbon materials were shown to have large surface areas and pore volumes as well as graphite-like character, so cyclic voltammetry (CV) was implemented on the ball-milled carbon materials to investigate the capacitive response. Figure 35 shows CV curves collected from the bare carbon tissue and an electrode prepared with 95:5 carbon black and Nafion polymer.

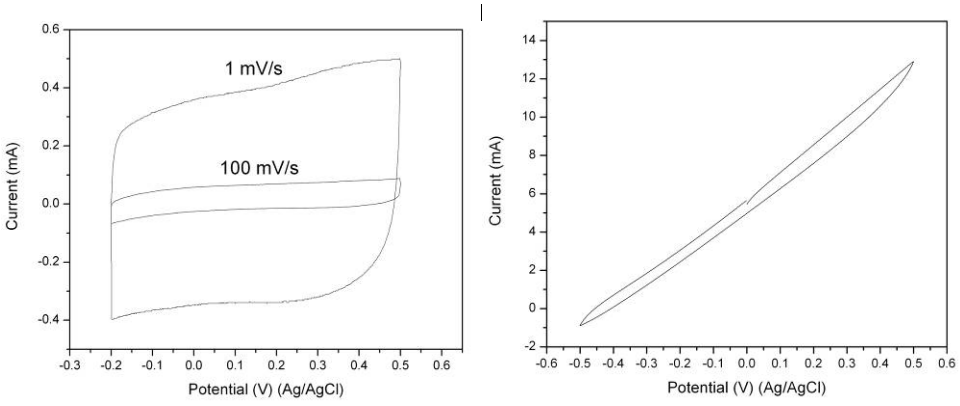

Figure 35. Cyclic voltammograms of the carbon tissue substrate and carbon black electrode.

The carbon tissue used as the substrate for attaching the prepared porous carbon shows an almost ideal capacitive response. The current is almost independent to the voltage applied with little pseudocapacitive influence. When only carbon black is used, a resistive response is seen in addition to capacitance. This suggests that the carbon particles are in poor electrical contact and the electrode preparation method is not ideal. The CV curves for the ball-milled carbon in aqueous and organic electrolyte are seen in Figure 36. Both of these experimental setups also show resistive current responses in addition to capacitive responses.

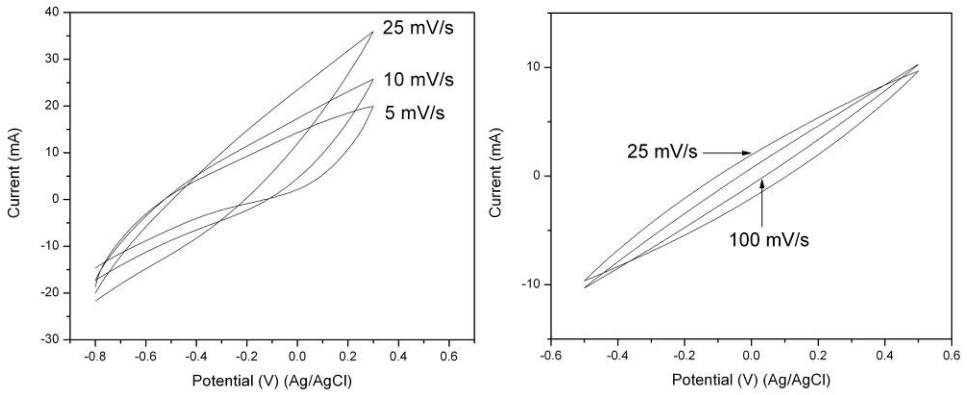

Figure 36. Cyclic voltammograms of the ball-milled carbon electrodes in aqueous and organic electrolyte.

The enhanced capacitive response due to the bill-milled carbon observed in the aqueous electrolyte is clear. There is a much larger capacitive current observed for all the scan rates. The electrode analyzed in organic electrolyte shows a symmetric response but smaller capacitive currents. The specific capacitances of all the prepared electrodes are tabulated at their different scan rates in Table 4.

Table 4. Specific capacitances at listed scan rates and potentials

Sample	Carbon Tissue		Carbon Black	Carbon (aqueous)			Carbon (organic)	
Scan Rate (mV/s)	10	100	100	5	10	25	25	100
Specific Capacitance (F/g)	0.0500	0.0415	1.49	172	90.1	32.3	3.66	0.338
Specific Capacitance (F/cm^3)	0.108	0.0892	3.20	82.0	43.0	15.4	1.75	0.161
Potential (V)	0.15	0.15	0.20	0.0	0.0	0.0	0.0	0.0

The carbon tissue substrate had the lowest resistivity leading to the most ideal capacitive response, but also the lowest surface area and therefore the lowest specific capacitance. Preparing an electrode of carbon black enhanced the specific capacitance by two orders of magnitude (BET surface area = 75 m^2/g), but the poor contact between the carbon black particles is likely the cause of the variable current response with changing potential. The electrodes with the ball-milled carbon show the highest specific capacitances when measured in vacuum infiltrated aqueous H_2SO_4 electrolyte and the highest capacitance of 172 F/g is measured when the scan rate is a relatively slow 5 mV/s. The capacitance then decreases with increased scan rate. This suggests capacitive phenomena occurring on several different time scales, with the slowest only being observable with the slowest scan rates. The electrodes were vacuum infiltrated because they did not spontaneously wet in the aqueous electrolyte. The prepared carbon is likely hydrophobic due to a lack of oxygen functional groups that enhance hydrophilicity.[68,69] The organic electrolyte was not vacuum infiltrated because it appeared to spontaneously wet upon immersion. This may have been a superficial infiltration into only the largest of pore spaces without any electrolyte

in contact with the smaller pore sizes where most of the measured surface area exists leading to low specific capacitances. Additionally, the concentration of the organic electrolyte was much lower than that of the aqueous system which can lead to higher solution resistances.

The best measured specific capacitance values of the prepared porous carbon material are only moderately impressive and can probably be improved in several ways. At a slow scan rate (but still used in commercial capacitor devices[120]) of 25 mV/s the specific capacitances measured were 32.3 F/g and 15.4 F/cm^3. There are many reports in the literature of specific capacitances greater than 100 F/g.[105,121] Based on the resistive response seen in the CVs, it is likely that the electrode preparation had a large influence on the measured values. Ruiz et al. have reported a decrease of measured capacitance on the use of ball milling of the active component[122] and the presence of a polymeric binder[122] used for electrode preparation. Additionally, the proposed orientation of the graphite crystallites in the porous structure could have a negative effect on the specific capacitance of the prepared material. It has been reported that much like the structural anisotropy present in graphite crystallites, there exists anisotropy of capacitance between the basal plane and the edge sites. The basal planes of graphite have lower specific capacitance, on the order of 1-20 μF/cm^2 and the edge sites near 50-70 μF/cm^2.[59,123] Based on the current analysis, the basal plane of the synthesized graphite-like crystallites would be exposed to the electrolyte solution and would be able to support far less charge per area than those in an edge-exposed orientation.

There are several strategies modifying the material synthesis and electrode preparation to improve the specific capacitance. Avoiding or minimizing the ball milling treatment may preserve the original connectivity and exploring different binder systems or strategies may reduce resistivity in the prepared electrodes. One fruitful synthetic parameter to vary may lie in increasing the polymer precursor concentration during synthesis to produce carbon walls thicker than those seen in the TEM images. Barbieri et al. reported that carbons with exceptionally thin pore walls, the electric potential may not decay to zero within the pore wall and when double-layers exist on both sides, a reduction in specific capacitance is seen relative to what is expected based on surface area measurements.[124] Having thicker pore walls could avoid this effect and would also provide for the geometric possibility of having graphite crystallites in an edge-exposed orientation for improved capacitance. Additionally, it would be beneficial to optimize the amount of macroporosity present to provide essential mass transport throughout the electrode, but not so much as to decrease the capacitance per volume. Large macropores are filled with heavy electrolyte solutions in real world devices and contribute little in the way of capacitance leading to devices that have poor volume specific capacitances.[125]

4.4 Conclusion

The presented method of interpenetrating inorganic/organic gel networks has been shown to be a scalable and facile method for the preparation of highly porous carbon with a recyclable template. The carbon was shown to contain a large

volume of mesopores and exhibit some crystallinity to provide for electrical conductivity. The carbon could be prepared into electrodes and was shown to exhibit promising capacitance values of 32.3 F/g and 15.4 F/cm^3 at reasonable potential scan rates of 25 mV/s. The flexibility of the synthetic method also allows for modification of the preparation procedure to enhance the capacitive response of the mesoporous carbon.

CHAPTER 5

HIERARCHICALLY POROUS CARBON

5.1 Introduction

Porous carbon is an important industrial material with many applications in energy storage, such as batteries and supercapacitors[68,102], as well as filtration, adsorption and catalysis. Carbon is particularly appealing for large scale application due to its earthly abundance, chemical robustness, and ecological friendliness, but also because it can be prepared as a high surface area and porosity material, which can enhance the effectiveness of the carbon in its various applications.

Porous carbon has been produced using a wide range of methods such as eco-oriented methods like thermally treating agricultural waste or otherwise abundant biomass to generate a carbon and applying an activation treatment to enhance porosity.[126,127] In many cases, these techniques generate predominantly microporous and/or macroporous carbons and lack fine control of the type and extent of porosity. Other synthetic techniques that demonstrate greater control over the porosity involve templating which make use of a temporary material distributed throughout a carbon precursor to provide pore space at their removal. Templates can be “soft” components like self-organizing molecules like block co-polymer systems and surfactants,[31,33,128] or “hard“ components which are previously existing solids. Particles can be dispersed or distributed throughout a carbon precursor solution and subsequently removed chemically.[129,130] Alternatively, an existing porous solid can be infiltrated with a carbon precursor,

pyrolyzed, and etched to generate a negative replica of the original non-carbonaceous solid.[131–133] In all templating methods, the textural control over the final porous product is predominantly determined by the textural control over the starting template material.

Soft templates are often used for the synthesis of porous carbon by proxy through the generation of an intermediate sacrificial material like porous silicas MCM-48 or SBA-15.[133] This hard template intermediate can then be infiltrated with a carbon-generating material, followed by a dissolution step to remove the porous oxide template and leave behind porous carbon. The incorporation of other particulate hard templates into a carbon forming matrix has its share of challenges as well. The particles are subject to certain size and density limits that allow them to remain dispersed or otherwise non-aggregated. Additional surface modification may be necessary to stabilize a suspension of colloidal templates to prevent aggregation and settling[134] or alternatively, aggregation can be avoided by careful monitoring of gelation times to predict the appropriate moment of template addition to a solution on the verge of gelling[135] to get well distributed templates.

A desirable material for the homogeneous dispersal of solids would be one that has a variable viscosity. Thixotropic materials exhibit a time dependant reduction in viscosity at the application of shear forces. At the removal of the shear force, the viscosity recovers after a certain time to return to a solid-like gel state.[136] Alumina gels are thixotropic materials such that the initial bulk gel can be liquefied, and given time, can reform into a bulk gel.[137] Pek et al. demonstrated

the use of a thixotropic polymer-silica nanocomposite as a means of homogeneously dispersing biological cells in a gel medium.[138] Here, the use of thixotropic gels as a method for homogeneous template dispersal as well as a template itself is reported. This method makes use of the thixotropic properties of alumina gels. The use of mechanical blending of the wet gels allows for the facile mixing and distribution of other matter to be incorporated into the composite. Optional post-treatment steps can be the removal of one or more of the components of the as-prepared composite. In this work, the metal oxide template materials are removed from the composite by chemical etching to provide porous carbon materials of high surface area and pore volume.

5.2 Experimental

5.2.1 Mesoporous Carbon Preparation

A bulk alumina wet gel was prepared following the epoxide-induced gelation method outlined by Baumann et al.[139] The precursors were mixed together and gelled in approximately one hour after which the gel was aged an additional hour. This bulk gel was divided into 5 portions and blended with aqueous ethanol solutions of resorcinol and formaldehyde of varying concentrations (at fixed molar ratio of R:F, 1:2).

Each sample blending was carried out using a handheld kitchen blender (Oster) on the lowest speed setting for about 3 minutes. The fluidic samples were then poured into molds to thixotropically gel within a few minutes. After regelation, the composite gels were left at room temperature for 24 hours

followed by heating at 70 °C for 3 days to promote the polymerization of the RF carbon precursors. The translucent red gel monoliths G-1 through G-5 were then removed from their molds and cut into centimeter-sized pieces and left to dry in air to produce composite xerogel pieces X-1 through X-5. The xerogels were then placed in a tube furnace and purged with argon gas for 15 minutes then heated at a rate of 2 °C/min and held at 110 °C for 1 hour under flowing argon. The furnace was then heated to 700 °C at a rate of 6 °C/min and held for 1 hour under flowing argon. The furnace was then allowed to cool ambiently and the metal oxide-carbon composite (MOCC) pieces M-1 through M-5 were removed from the furnace.

To produce porous carbon C-1 through C-5, the alumina component was removed from the MOCCs M-1 through M-5 by hydrothermal treatment in H_2SO_4. Each MOCC sample was loaded into aTeflon lined Parr bomb charged with 9 g of 32 % w/w H_2SO_4, sealed and heated at 160 °C for 4 days. The porous carbon samples were removed from the Parr bombs and rinsed with 32 % w/w H_2SO_4 several times and then with deionized water until the wash solution was pH 7.

5.2.2 Hierarchically Porous Carbon Preparation

A bulk alumina gel was prepared using the same epoxide method as outlined above. For this preparation, 5.68 g $AlCl_3 \cdot 6H_2O$ (Sigma-Aldrich) was dissolved in 35 ml of 50/50 volume mixture of absolute ethanol (Tarr) and deionized water followed by the addition of 13.6 g of propylene oxide (Alfa Aesar). The solution was mixed thoroughly and allowed to gel for 1 hour. An 11.3 g portion of this

bulk wet alumina gel was placed in a 20 ml Ultra Turrax Tube (IKA) with an RF solution consisting of 0.442 g of resorcinol (Sigma-Aldrich) and 0.667 g of 37 % formaldehyde solution (Sigma-Aldrich) dissolved in 3.5 ml of 50/50 volume mixture of ethanol and deionized water. This mixture was blended with 1.11 g copper particles (-625 mesh, Alfa Aesar) at 6000 rpm two times for 60 seconds. This mixture was poured into molds, sealed and left at room temperature for 1 day. The molds were then heated at 70 °C for 1 day, followed by opening of the molds and for air drying to generate composite xerogels. The xerogels were removed from their molds, placed in a tube furnace and purged with argon gas for 15 minutes then heated at a rate of 2 °C/min and held at 110 °C for 1 hour under flowing argon. The furnace was then heated to 700 °C at a rate of 4 °C/min and held for 1 hour under flowing argon. The furnace was then allowed to cool ambiently and the alumina/copper/carbon composite materials were removed from the furnace.

The composite pieces were then broken into ~ 1 mm^3 sized pieces and placed in a centrifuge tube with a stir bar. The sample tube was then filled with 1.7 g ethylenediaminetetraacetic acid (EDTA) dissolved in 40 ml of H_2O and 0.5 ml of H_2O_2. This was placed in a water bath on a stir plate and heated to ~ 70 °C with magnetic stirring. After several hours, the solution was blue, indicating the dissolution of the copper metal. After becoming dark blue, the sample tube was centrifuged at 4000 rpm for 10 minutes and decanted. The EDTA/H_2O/H_2O_2 solution was replaced over the composite pieces and returned to the heated water bath with stirring. The solution was changed in this manner 8 times over 2 weeks.

After the final solution exchange, the particles were vacuum filtered over a fine glass frit filter and washed thoroughly with deionized water. The alumina/carbon composite particles were then hydrothermally treated in a Parr bomb charged with 32 % w/w H_2SO_4 and heated to 160 °C for about 20 hours. The carbon particles were then removed from the bomb and centrifuged at 4000 rpm for 10 minutes. The particles were then successively washed with 32 % w/w H_2SO_4, deionized water, and acetone with centrifugation between each wash step. Finally, the carbon particles were dried in air.

5.2.3 Materials Characterization

Transmission electron microscopy (TEM) was performed on a JEOL JEM 2000FX operating at 200 kV. The TEM samples were prepared by grinding in an agate mortar in ethanol and dispersing the ground particles in ethanol. A copper grid covered with a holey carbon film was dipped in the solution, removed, and air dried.

The scanning electron microscopy (SEM) images were collected on an FEI XL-30 E-SEM. The SEM samples were prepared by grinding and dusting the sample onto sticky carbon tape on an SEM sample stage.

The porosity and surface areas were characterized using N_2-sorption/desorption data collected by a Micromeritics ASAP 2020 volumetric adsorption analyzer at 77 K. Prior to the analysis, samples were heated to 300 °C for about 8 hours under vacuum with a residual pressure of ≤ 5 μmHg. Specific areas were calculated according to the BET equation, using the adsorption branch

in the relative pressure range of 0.05 to 0.2. For the calculation of total pore volume, the desorption branch was considered and the pore volume was obtained from the amount of nitrogen adsorbed at a $P/P_o = 0.97$. Pore size distributions were obtained using the Barrett-Joyner-Halenda (BJH) method with the Carbon Black STSA thickness curve (ASTM D-6556-0lA) and Faass[83] correction on the adsorption branch assuming a cylindrical pore model with all pores open at both ends. For porous carbons, the thickness equation used for the t-plot calculations was also Carbon Black STSA.

The Raman data were collected from ground powder samples using a custom built Raman spectrometer in a 180 ° geometry setup. The sample was excited using a 100 mW Compass 532 nm laser. A neutral density filters were used to reduce the laser power to 5 milliwatts. The laser was focused onto the sample using a 50X super long working distance Mitutoyo objective with a numerical aperture of 0.42. The signal was discriminated from the laser excitation using a Kaiser laser band pass filter followed by a Semrock edge filter. The data were collected using an Acton 300i spectrograph and a back thinned Princeton Instruments liquid nitrogen cooled CCD detector.

The TGA data were collected on a Mettler Toledo TGA DSC 1 STARe system. Samples were analyzed by heating from 25 °C to 300 °C at 10 °/min and holding at 300 °C for 15 minutes followed by heating to 1000 °C at 20 °C/min and holding for 15 minutes. All analysis was done under air flow at 50 ml/min.

5.3 Results and discussion

5.3.1 Mesoporous Carbon

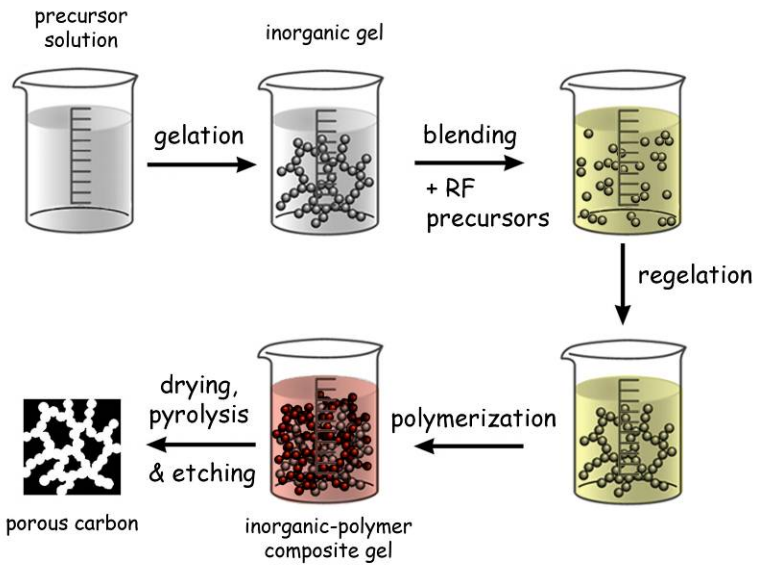

Figure 37. General synthetic method for porous carbon from thixotropic alumina gels.

A series of thixotropic alumina gels was blended with varying concentrations of monomeric carbon precursors followed by treatments to favor polymerization, drying, pyrolysis, and oxide etching to provide porous carbon materials of different morphological consequence as depicted in Figure 37. During the preparation of the target porous carbons, the various intermediate porous materials that were generated were also analyzed.

The first porous materials generated were the amorphous composite xerogels consisting of interpenetrating networks of RF polymer and alumina gel. Table 5 shows the calculated values from the collected nitrogen sorption data which show a decrease in specific surface area and pore volume with increasing carbon precursor concentration.

Table 5. Xerogel surface area and pore characteristics

Xerogels	Resorcinol concentration (M)	BET surface area[a] (m^2/g)	Pore Volume[b] (cm^3/g)	Average Pore Size[c] (nm)
X-1	0.110	268.0	0.280	4.18
X-2	0.324	182.1	0.198	4.34
X-3	0.533	128.1	0.159	4.96
X-4	0.752	76.26	0.097	5.08
X-5	0.990	40.29	0.047	4.67

[a] Pressure range $P/P_o = 0.05\text{-}0.2$
[b] Single point desorption nearest $P/P_o = 0.97$
[c] 4V/A (BET)

This could be interpreted as the inorganic template network having characteristic pore structure that is filled to varying extents with the polymeric carbon precursors. The lowest concentration sample has a thin coating of polymeric material throughout the inorganic template while the highest concentration sample has a thick coating that decreases the overall surface area (due to the effective increase of the primary particle size) as well as possibly blocking pores. But the increase in carbon precursor concentration also increases the structural robustness of the composite xerogels as evidenced by an observed reduction in the shrinkage of the composite gels during drying. This is supported by the slight and general increase in average pore size from samples X-1 to X-5.

Other information regarding the prepared materials is revealed through the examination of the N_2-sorption isotherms and the calculated BJH pore size distribution plots shown in Figure 38 and Figure 39 respectively.

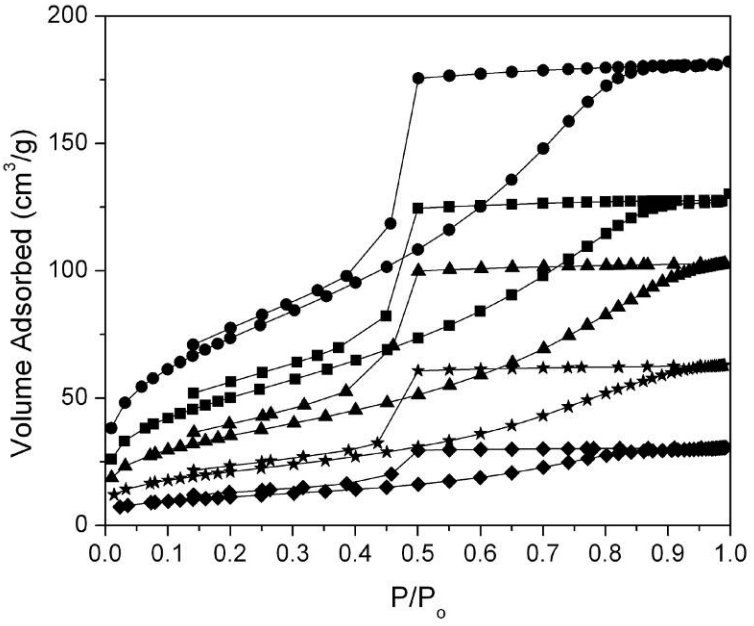

Figure 38. Isotherms of xerogel composites X-1 (●), X-2 (■), X-3 (▲), X-4 (★), X-5 (◆).

The xerogel isotherms exhibit low pressure hysteresis at P/P_o less than 0.4. This may indicate the entrapment of N_2 molecules within pores of comparable size to the adsorptive or the swelling of the porous structure during the measurement.[67] The latter may be a possibility due to the non-rigidity of either amorphous component as evidenced by the ability of the composite wet gel to shrink to a monolithic composite xerogel. Because the hysteresis loops are type H2 and lack hysteresis loop closure, the adsorption band was used for all BJH calculations for the xerogel composites.

The BJH pore size distributions for the xerogel samples in Figure 39 show the presence of a range of approximately the same size pores with a slight shift towards larger pore sizes and periodic decrease in pore volume with higher carbon precursor concentration. Both of these trends can be corroborated by the previous

conjecture of increasing polymer layer thickness and the blocking of pores with increased polymer content.

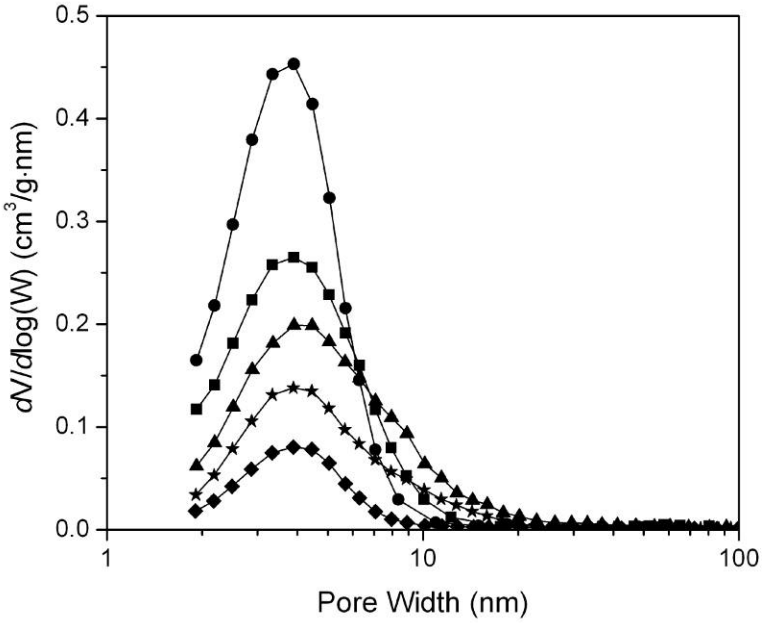

Figure 39. BJH pore size distributions for X-1 (●), X-2 (■), X-3 (▲), X-4 (★), X-5 (◆).

After analysis, the amorphous xerogel composites were processed further to generate the subsequent porous MOCCs and carbons.

The MOCCs resulting from the pyrolysis of the amorphous composite xerogels were also analyzed by gas adsorption methods in a similar manner as the amorphous xerogel composites. The collected isotherms of the MOCCs are shown in Figure 40 and show the same trend as the amorphous xerogel composites with a decrease in total gas adsorbed as the polymer precursor concentration is increased.

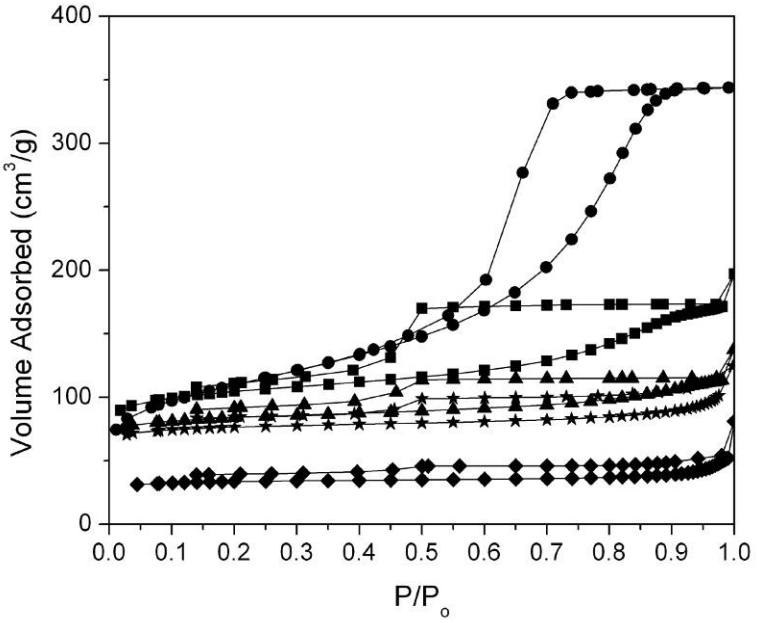

Figure 40. Isotherms of MOCCs M-1 (●), M-2 (■), M-3 (▲), M-4 (★), M-5 (◆).

The presented view of wall-thickening and pore filling with increasing carbon precursor concentration can be further supported by the examination of the gas adsorption and TGA data collected from the MOCC samples shown in Table 6.

Table 6. Surface area and pore characteristics of MOCC materials

Sample	Resorcinol concentration (M)	BET surface area[a] (m^2/g)	Pore Volume[b] (cm^3/g)	Average Pore Size[c] (nm)	Weight % Carbon	Weight % Alumina	Average Density[d] (g/cm^3)	Porosity[e] (%)
M-1	0.110	390.9	0.532	5.44	38.6	61.4	2.86	60.3
M-2	0.324	364.6	0.268	2.94	63.0	37.0	2.53	40.4
M-3	0.533	300.9	0.178	2.37	74.6	25.4	2.40	29.9
M-4	0.752	274.9	0.174	2.53	78.7	21.3	2.35	29.0
M-5	0.990	123.8	0.0837	2.71	81.6	18.4	2.32	16.3

[a] Pressure range $P/P_o = 0.05\text{-}0.2$

[b] Single point desorption nearest $P/P_o = 0.97$

[c] 4V/A (BET)

[d] Average density calculated by $\dfrac{w_{loss} + w_{residue}}{\left(\dfrac{w_{loss}}{\rho_{carbon}} + \dfrac{w_{residue}}{\rho_{\gamma-alumina}} \right)}$

where $\rho_{carbon} = 2.15 g/cm^3$ and $\rho_{\gamma\text{-alumina}} = 3.6 g/cm^3$

[e] $$porosity = \left(\frac{PoreVolume}{PoreVolume + \frac{1}{\rho_{Avg}}} \right)$$

The MOCC samples contain both the inorganic oxide network and the porous carbon network and show the same general trends as the amorphous composite xerogels of decreasing BET surface area and pore volume with increasing carbon precursor concentration. Thermogravimetric analysis was also done on the samples to determine the relative masses of carbon and aluminum oxide present. The relative mass of carbon increases with the carbon precursor content, as expected. These relative masses can be used to calculate an average solid density which can be assumed to be the "true" density[140] where only the volumes of the solid components are considered while excluding pores and interparticle voids.

This true density can then be used with the pore volume measured from N_2-sorption measurements to calculate a percent porosity. It can be seen that the change in porosity with increasing carbon precursor concentration is quite severe, decreasing from ~60-16%. The areas underneath the BJH pore distribution curves in Figure 41 calculated from the MOCC isotherms are indicative of the total pore volumes and highlight this disparity.

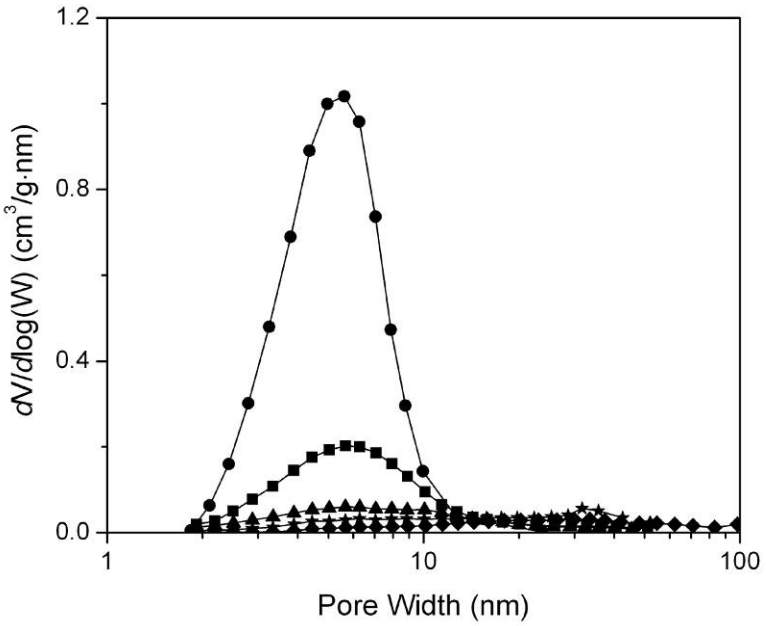

Figure 41. BJH pore size distributions of samples M-1 (●), M-2 (■), M-3 (▲), M-4 (★), M-5 (◆).

The M-1 sample shows rather high porosity after pyrolysis and before oxide removal, which is somewhat surprising for a xerogel prepared from a sol-gel method. This suggests that having a small quantity of the polymer present during composite gel drying is conducive to pore preservation and avoiding pore collapse. Without special treatment, most gels prepared by the sol-gel method are susceptible to being destroyed by capillary forces that occur during evaporative

drying.[20] It was noted that during the composite gel drying step prior to pyrolysis, the gels exhibited reduced shrinkage with increasing carbon precursor concentration. This supports the hypothesis that the pores are progressively filled with increasing carbon precursor polymer and ultimately buttress the composite porous structure against collapse.

Figure 42 shows TEM micrographs of the MOCC sample M-1 produced from the lowest polymer precursor concentration sample and the result of removing various components.

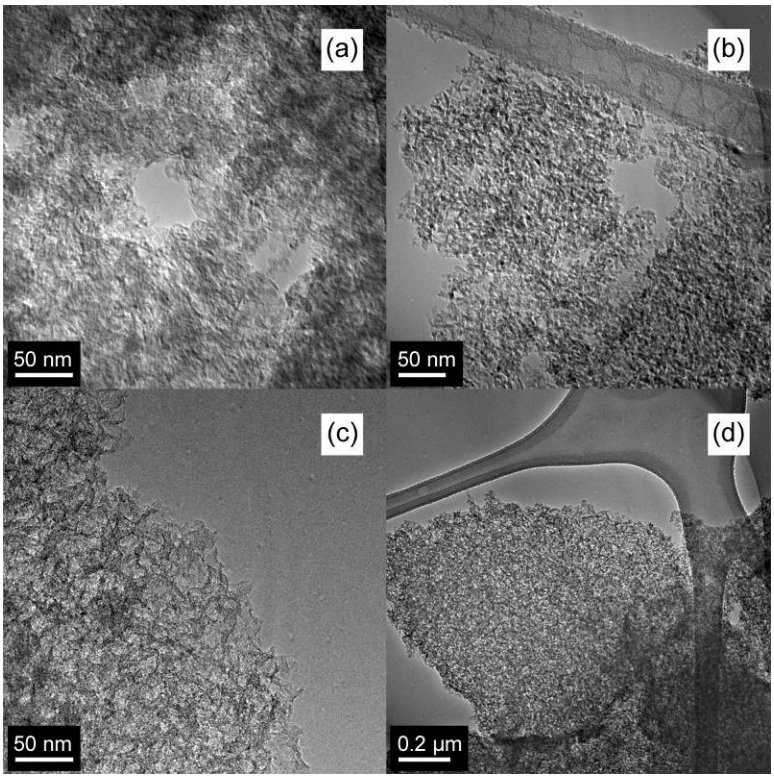

Figure 42. TEM images of (a) composite M-1, (b) porous alumina from burning M-1, and porous carbon C-1 at (c) high magnification and (d) low magnification.

The complete MOCC material is shown in Figure 42a where macropores can be seen amongst an intimate mixture of aluminum oxide and carbon. The structure of this complex material is clarified when comparing the complimentary materials

shown in Figure 42b and c. Figure 42b is the resulting porous alumina left behind after burning away the carbon in the composite material shown in Figure 42a. Anisotropic alumina particles can be seen, which are characteristic of calcined alumina gels prepared from aluminum chloride precursors.[19,139] These particles are sintered together forming a solid arrangement with a continuous network of pores throughout. If, instead, the MOCC material in Figure 42a is chemically treated to remove the alumina, a porous carbon material is produced as shown in Figure 42c-d. An interconnected network of large disordered mesopores can be seen between the thin carbon walls. Because a continuous inorganic gel structure is used as a template for the polymerizing carbon precursors, a bi-continuous network of organic and inorganic components can be ensured given that the dilution of one component by the other is not at either extreme. Thusly, upon removal of either component, a continuous open porosity throughout a continuous remaining solid can be ensured. This continuity is demonstrated by the large, millimeter-size particles of porous carbon shown in Figure 43.

Figure 43. Photograph of the resulting porous carbon pieces

The scanning electron microscopy images in Figure 44 also show the macroscale angular faces indicative of the long range continuity present in the porous carbon particles as well as the finer mesoporous structure previously observed in the TEM images.

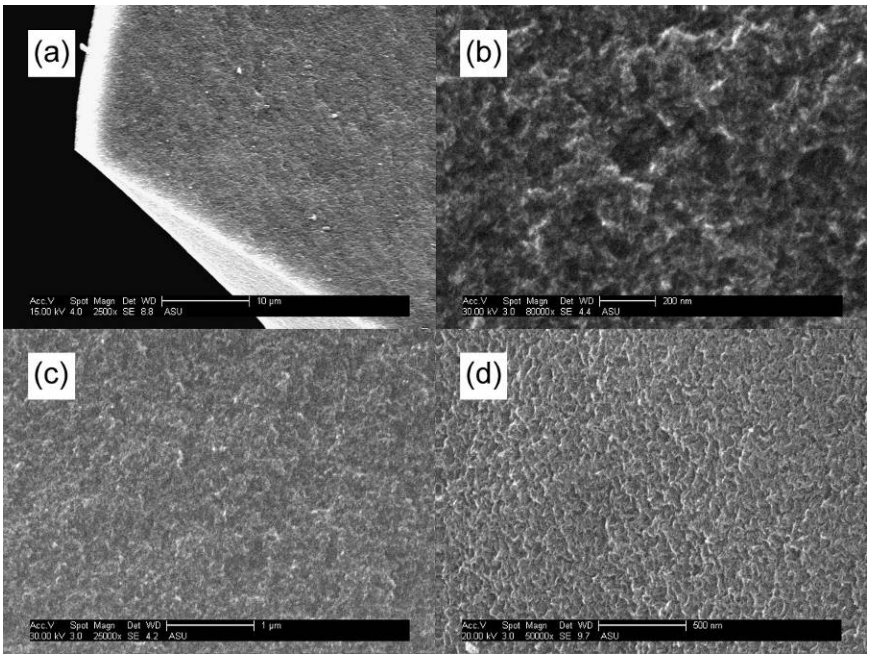

Figure 44. SEM images of M-1 at (a) low magnification (b) high magnification, and the resulting porous carbon C-1 after alumina removal (c) and (d)

The results of thermogravimetric analysis done on the MOCC samples prior to the etching step and on the porous carbon samples after the etching step to determine the extent of inorganic component removal are shown in Figure 45.

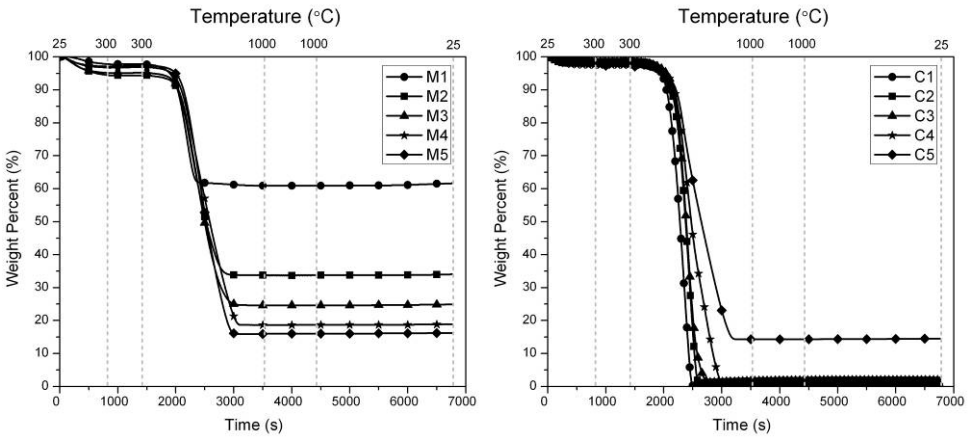

Figure 45. Thermogravimetric analysis of MOCC samples and carbon samples

The data show that essentially all of the alumina was removed from samples C-1 through C-4 with most of the alumina remaining within the C-5 sample that was present in the un-etched M-5 sample. It could be possible that the alumina template in M-5 was so inundated by the high content of carbon precursors that the template particles were thickly covered or otherwise practically separated to such an extent to frustrate template removal by dissolution. The gas adsorption data in Table 6 shows that sample M-5 had very little accessible pore volume and low surface area relative to the other 4 composites, which could frustrate the kinetics of dissolution greatly.

The series of porous carbon materials C-1 through C-5 were also analyzed by N_2-sorption methods. The carbon samples show reduced adsorption capacity with increasing carbon precursor concentration as seen in Figure 46 which is the same trend seen in the preceding samples.

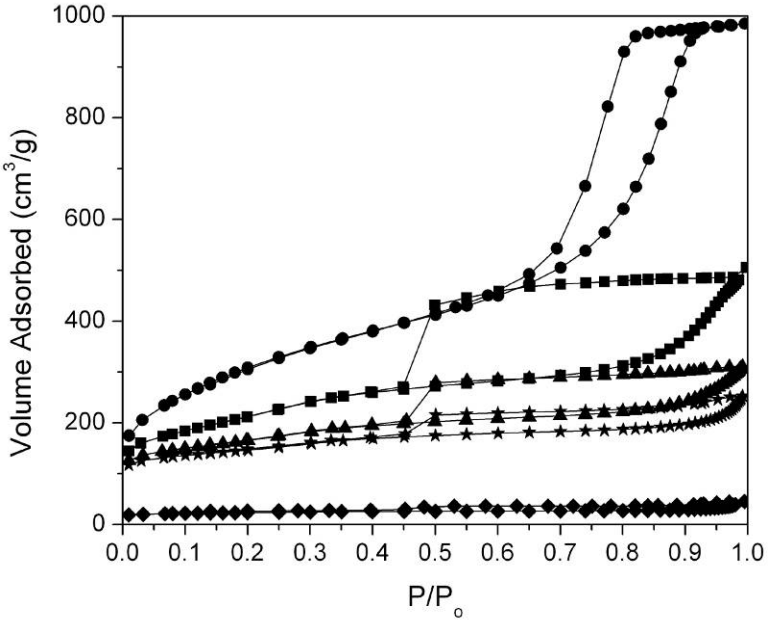

Figure 46. Isotherms of carbon samples C-1 (●), C-2 (■), C-3 (▲), C-4 (★), C-5 (◆).

The isotherm for C-1 shows a hysteresis loop of type H1, while samples C-2 through C-5 show H2 type loops. This indicates that carbons C-2 through C-5 likely suffer from the pore blocking or percolation effects. The isotherm data were interpreted through the use of the BET, BJH, and t-plot methods, the results of which are shown in Table 7.

Table 7. Surface area and pore characteristics for porous carbon samples

Sample	Resorcinol Concentration (M)	BET Surface Area (m^2/g)[a]	Pore Volume (cm^3/g)[b]	Average Pore Size (nm)[c]	Micropore Surface Area (m^2/g)[d]	% Micropore Surface Area	BET C value
C-1	0.110	1138	1.52	5.34	49.7	4.4	69
C-2	0.323	751.8	0.752	4.00	106.5	14.2	224
C-3	0.530	571.7	0.479	3.35	213.8	37.4	-386
C-4	0.746	501.1	0.388	3.10	257.1	51.3	-166
C-5[e]	0.980	80.27	0.068	3.42	52.4	65.3	-138

[a] Pressure range $P/P_o = 0.05\text{-}0.2$
[b] Single point desorption nearest $P/P_o = 0.97$
[c] 4V/A (BET)
[d] t-plot fit for thickness range of 0.35-0.5 nm
[e] Did not have the oxide fully removed

Two clear trends that can be observed are the decrease in BET surface area and total pore volume with increasing carbon precursor concentration. This can be interpreted with the observation that the RF polymerization step appears to be catalyzed by the inorganic gel surface, which has been reported in similar composite systems in literature.[141] This mechanism appears to favor the formation of polymer layers on the surface of the inorganic gel, the thickness of which increases with higher polymer precursor concentration. Correspondingly thick layers of carbon are formed upon pyrolysis of the composite material. The lowest carbon precursor concentration sample, C-1, has only very thin pore walls as seen in Figure 42c, which provide for the highest specific surface area and pore volume. The thickening of these walls with increased polymer content results in lower specific surface area due to the effective increase of the primary composite particle size. Additionally, the same inorganic gel template is used for all samples, so the inter-particle pore space is encroached upon by the thicker walls or

otherwise filled or blocked, resulting in reduced specific pore volume. This reduction in pore volume with increased polymer content has been observed for all previous samples.

This reduction in pore space is shown for the porous carbons in the BJH pore size distribution in Figure 47 as well as the continuous reduction of the average pore size for samples C-1 through C-4 shown in Table 7.

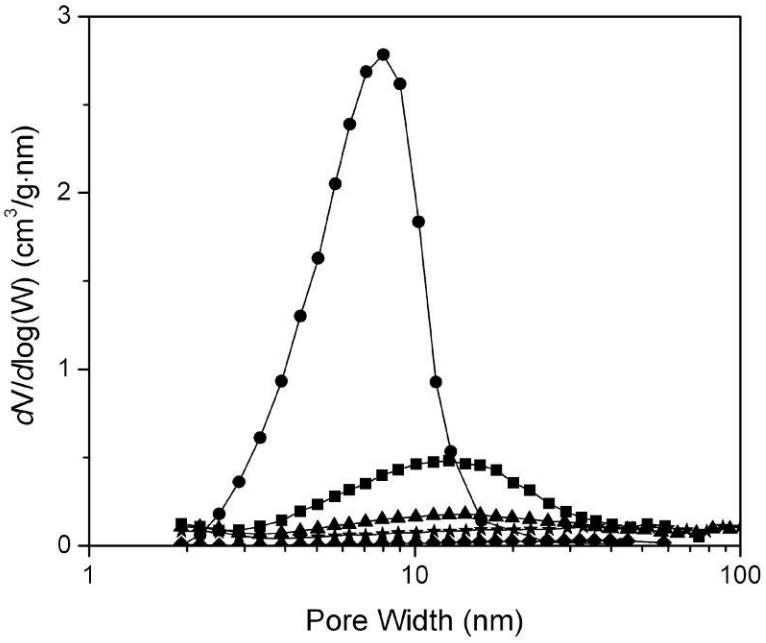

Figure 47. BJH pore size distributions for samples C-1 (●), C-2 (■), C-3 (▲), C-4 (★), C-5 (◆).

The presence of microporosity was also indicated from the gas adsorption experiments and the resulting analysis with the t-plot method. The BET C values shown in Table 7 are proportional to the slope of their respective BET plots and inversely proportional to the intercepts. Large BET C values are indicative of high adsorbate/adsorbent interactions[17] which arise when surfaces are energetically inhomogeneous or when physisorption occurs in pores of molecular

dimensions, i.e. micropores.[140] In the porous carbon samples, the slope of the BET plots (not shown) increase with increased carbon precursor concentration, initially having a positive intercept and ultimately a negative intercept. This suggests an increase in microporosity with carbon precursor concentration. While negative BET C values indicate that the pressure range used for the BET equation is invalid, following the suggestions of Rouquerol et al.[142] for applying the BET equation to microporous materials results in BET surface areas that were no more than 10% greater than those calculated using the range P/P_o = 0.05-0.2 with all physical trends remaining the same, so the traditional pressure range was used for the relative comparison. The t-plot method was also used to calculate the relative contribution of the microporosity to the total surface area. The amount of specific surface area from micropores increases with carbon precursor concentration as well as the relative contribution of micropore surface area to the total surface area. This can be rationalized using the same wall thickening hypothesis as proposed previously. The thin carbon walls in sample C-1 contain a small number of micropores, but the overall structure is predominantly mesoporous. As the carbon precursor concentration is increased, the resulting carbon walls can fill or block mesopores of increasing size while providing more carbon volume to harbor the non-templated micropores. This scenario would result in an overall decrease in specific surface area and pore volume due to mesopore filling/blocking while simultaneously increasing the relative amount of microporosity.

Raman data were collected for the C-1 carbon pyrolyzed at 700 °C as well as a sample pyrolyzed at 1000 °C to investigate the extent of graphitization. The

collected data showed both the D and G bands at ~1360 and 1580 cm^{-1} as shown in Figure 48.

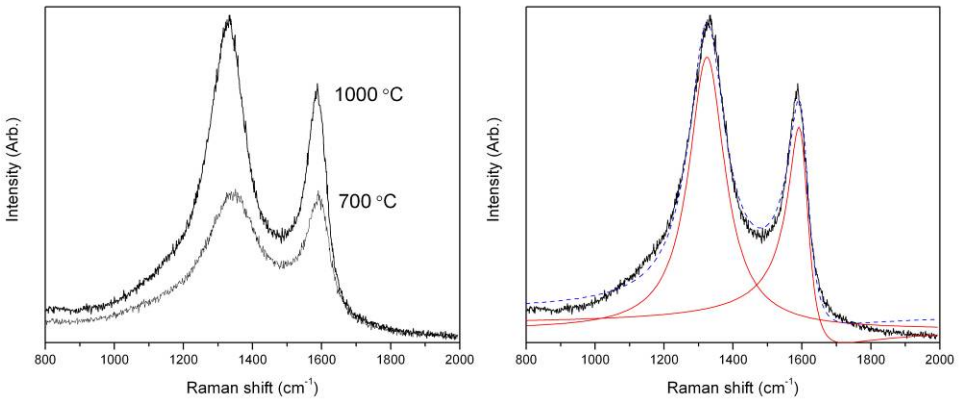

Figure 48. Raman data for carbons treated at different temperatures. Also shown is the fitted lineshape (dashed line) of 1000 °C carbon for determining relative peak intensities.

A pure graphite large crystal exhibits only a narrow G band corresponding to C-C E_{2g} stretching mode. Less crystalline, and generally lower temperature treated carbons include the D band corresponding to a usually forbidden A_{1g} breathing mode present in finite and disordered graphite crystallites.[119] As shown in Chapter 4, the ratio of the intensities of the D and G bands can be used to estimate the lateral dimensions of the graphite-like crystallites according to

$$\frac{I(D)}{I(G)} = \frac{4.4nm}{L_a} \qquad (1)$$

where L_a is the lower bound diameter of the crystallite for a sample investigated with a laser of lower energy than 488nm. The peak intensites were determined following the suggestions of Ferrari and Robertson by fitting a Breit-Wigner-Fano line to the G peak and a Lorentzian line to the D peak as shown in Figure 48.[119] Using equation 1 with a measured I(D)/I(G) of 1.40 collected using a 532 nm laser for the carbon treated at 1000 °C generates a lower bound for crystallite size

of about 3.1 nm. However, a I(D)/I(G) ratio of 1.08 for the 700 °C carbon would generate a larger crystallite size of about 4.1 nm. This carbon likely lies in the lower size regime as outlined by Ferrari and Robertson[119] where I(D)/I(G) is proportional to L_a^2 rather than $1/L_a$ and a value of 1.08 corresponds to a crystallite size of approximately 1.4 nm.

5.3.2 Hierarchically Porous Carbon

Figure 49 shows SEM images of the hierarchically porous carbon prepared using a macroporogen.

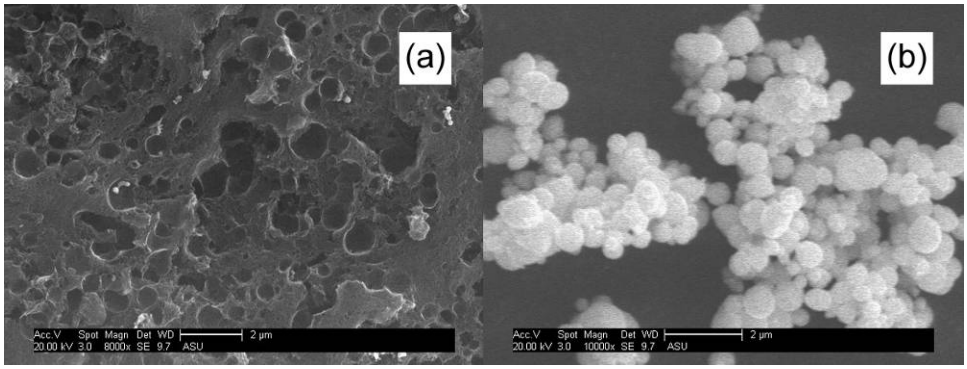

Figure 49. SEM images of hierarchically porous carbon and copper particle templates.

The pore spaces left behind by the copper particles can be seen in Figure 49a ranging from tens to hundreds of nanometers in diameter and the copper particles themselves are seen in Figure 49b. The ability to homogeneously distribute the dense metal particles throughout the samples exhibits one of the advantages of the thixotropic method outlined here. The TEM images shown in Figure 50 exhibit the same sphere shaped macropores as seen in the SEM images, but the fine mesostructure produced by the removal of the alumina template can also be seen.

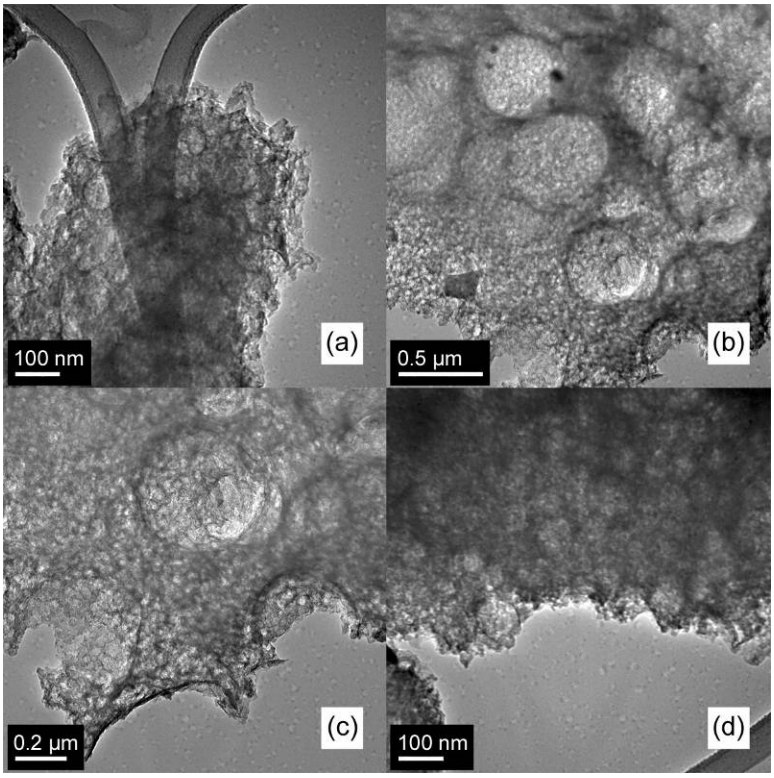

Figure 50. TEM of hierarchically porous carbon after removal of all templates.

Mesoporous carbons can be produced easily by this method, but it is shown that macroporogens can also be included with facility without needing careful manipulation as required by many self-structuring or self-organizing techniques. The high viscosity recovery rate of the thixotropic medium after blending allows the dispersal of a variety of macroporogens (as well as other non-template solids) of high bulk density without the issue of the templates settling or otherwise inhomogeneously segregating in the bulk composite.

The N_2-sorption isotherms and BJH pore size distributions for the hierarchically porous carbon after template removal and an analogous mesoporous carbon that did not have a macroporogen included during preparation are shown in Figure 51.

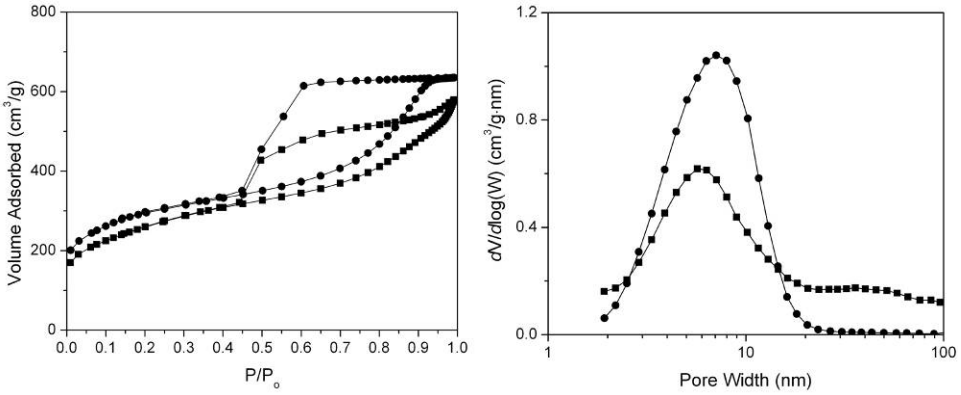

Figure 51. N_2-sorption isotherms and BJH pore size distributions of the mesoporous (●) and hierarchically porous carbon samples (■).

The isotherms for the mesoporous carbon and hierarchically porous carbon are both type IV isotherms with hysteresis loops of mostly type H2 character. Most notably, however, the hierarchically porous carbon shows a lack of a plateau region at high P/Po suggesting a continuous distribution of pores extending from the mesopore region into the macropore region, which can be seen in the BJH pore size distribution plot. Also noticeable in the BJH pore size distribution plot is the reduction in mesoporosity when the macroporogen is included. The inclusion of the macroporogen displaces a rather large volume of mesoporous carbon, and upon the removal of the templates, large porous voids are left where mesostructured carbon would have existed had the macroporogen been excluded from the synthesis altogether.

Table 8 shows the N_2-sorption results for the additional MOCC material prepared and the corresponding preparation with the incorporation and subsequent removal of copper macroporogen templates.

Table 8. Comparison of surface area and pore characteristics before and after template removal

	Resorcinol Concentration (M)	BET Surface Area[a] (m^2/g)	Pore Volume[b] (cm^3/g)	Average Pore Size[c] (nm)
Composite	0.26	379.6	0.349	3.67
Alumina	0.26	253.0	1.11	17.5
Mesoporous carbon	0.26	1057	0.982	3.71
Hierarchically porous carbon	0.25	924.4	0.886	3.83

[a] Pressure range $P/P_o = 0.05\text{-}0.2$
[b] Single point desorption nearest $P/P_o = 0.97$
[c] 4V/A (BET)

Comparing the mesoporous carbon and hierarchically porous carbon, it can be seen that there is an increase in average pore size when the copper template is used. The hierarchically porous carbon sample has a lower specific pore volume than the mesoporous carbon. This is a consequence of the copper particles being several hundred nanometers in diameter and generating pores of similar dimension. Pores of this size are outside the measurable limit for gas adsorption methods and are thus not measured as contributing to the total pore volume. However, the mesoporous carbon that is ultimately displaced by the copper particles contains pore that are of appropriate size to be measured by gas adsorption, and therefore contribute to the total pore volume.

5.4 Conclusion

Thixotropic alumina gels were used as a template for generating high surface areas and pore volumes in a series of carbon materials. The samples with higher carbon precursor concentrations in the solution added to the thixotropic gel

resulted in carbons with low surface areas and pore volumes. However, decreasing the carbon content allowed for the production of high surface area and highly mesoporous carbons. The thixotropic property of the gels was also successfully implemented as a facile means to generate hierarchically porous carbons by homogeneously incorporating large templates to introduce macroporosity in the final carbon materials.

REFERENCES

(1) Donnet, J.-B.; Bansal, R. C.; Wang, M.-J. *Carbon Black: Science and Technology*; Dekker: New York, 1993.

(2) Mattia, D.; Rossi, M. P.; Kim, B. M.; Korneva, G.; Bau, H. H.; Gogotsi, Y. *J. Phys. Chem. B* **2006**, *110*, 9850–9855.

(3) Gordon, R. G. *MRS Bulletin* **2000**, *25*, 52–57.

(4) Arai, T. *J. Phys. Soc. Jpn.* **1960**, *15*, 916–927.

(5) Batzill, M.; Diebold, U. *Progress in Surface Science* **2005**, *79*, 47–154.

(6) Thangaraju, B. *Thin Solid Films* **2002**, *402*, 71–78.

(7) Kuku, T. A. *Thin Solid Films* **1986**, *142*, 241–250.

(8) He, Y.-S.; Campbell, J. C.; Murphy, R. C.; Arendt, M. F.; Swinnea, J. S. *Journal of Materials Research* **1993**, *8*, 3131–3134.

(9) Bolzan, A. A.; Fong, C.; Kennedy, B. J.; Howard, C. J. *Acta Crystallographica Section B Structural Science* **1997**, *53*, 373–380.

(10) Pajonk, G. M. *Applied Catalysis* **1991**, *72*, 217–266.

(11) Rao, Y.; Antonelli, D. M. *J. Mater. Chem.* **2009**, *19*, 1937–1944.

(12) Hasegawa, G.; Ishihara, Y.; Kanamori, K.; Miyazaki, K.; Yamada, Y.; Nakanishi, K.; Abe, T. *Chem. Mater.* **2011**, *23*, 5208–5216.

(13) Petricevic, R.; Glora, M.; Fricke, J. *Carbon* **2001**, *39*, 857–867.

(14) Knox, J. H.; Kaur, B.; Millward, G. R. *Journal of Chromatography A* **1986**, *352*, 3–25.

(15) Rolison, D. R. *Science* **2003**, *299*, 1698–1701.

(16) Sarkisov, L. *Advanced Materials* **2012**, *24*, 3130–3133.

(17) Sing, K. S. W.; Everett, D. H.; Haul, R. A. W.; Moscou, L.; Pierotti, R. A.; Rouquerol, J.; Siemieniewska, T. *Pure and Applied Chemistry* **1985**, *57*, 603–619.

(18) Lu, G. Q.; Zhao, G. X. S. *Nanoporous Materials: Science and Engineering*; Imperial College Press, 2004.

(19) Ladd, D. M.; Volosin, A.; Seo, D.-K. *J. Mater. Chem.* **2010**, *20*, 5923.

(20) Brinker, C. J.; Scherer, G. W. *Sol-Gel Science: The Physics and Chemistry of Sol-Gel Processing*; Gulf Professional Publishing, 1990.

(21) Rolison, D. R.; Dunn, B. *J. Mater. Chem.* **2001**, *11*, 963–980.

(22) Parmenter, K. E.; Milstein, F. *Journal of Non-Crystalline Solids* **1998**, *223*, 179–189.

(23) Prakash, S. S.; Brinker, C. J.; Hurd, A. J.; Rao, S. M. **1995**, *374*, 439–443.

(24) Livage, J.; Henry, M.; Sanchez, C. *Progress in Solid State Chemistry* **1988**, *18*, 259–341.

(25) Hörtz, C.; Ladd, D. M.; Seo, D.-K. *MRS Online Proceedings Library* **2011**, *1306*.

(26) Guglielmi, M.; Menegazzo, E.; Paolizzi, M.; Gasparro, G.; Ganz, D.; Pütz, J.; Aegerter, M. A.; Hubert-Pfalzgraf, L.; Pascual, C.; Durán, A.; Willems, H. X.; Van Bommel, M.; Büttgenbach, L.; Costa, L. *Journal of Sol-Gel Science and Technology* **1998**, *13*, 679–683.

(27) Pekala, R. W.; Alviso, C. T.; Kong, F. M.; Hulsey, S. S. *Journal of Non-Crystalline Solids* **1992**, *145*, 90–98.

(28) Pekala, R. W. *Journal of Materials Science* **1989**, *24*, 3221–3227.

(29) Al-Muhtaseb, S. A.; Ritter, J. A. *Advanced Materials* **2003**, *15*, 101–114.

(30) Shi, Y.; Wan, Y.; Zhao, D. *Chemical Society Reviews* **2011**, *40*, 3854.

(31) Kresge, C. T.; Leonowicz, M. E.; Roth, W. J.; Vartuli, J. C.; Beck, J. S. *Nature* **1992**, *359*, 710–712.

(32) Beck, J. S.; Vartuli, J. C.; Roth, W. J.; Leonowicz, M. E.; Kresge, C. T.; Schmitt, K. D.; Chu, C. T. W.; Olson, D. H.; Sheppard, E. W. *Journal of the American Chemical Society* **1992**, *114*, 10834–10843.

(33) Zhao, D.; Feng, J.; Huo, Q.; Melosh, N.; Fredrickson, G. H.; Chmelka, B. F.; Stucky, G. D. *Science* **1998**, *279*, 548–552.

(34) Kim, H.-C.; Park, S.-M.; Hinsberg, W. D. *Chemical Reviews* **2010**, *110*, 146–177.

(35) Wang, Y.; Ma, C.; Sun, X.; Li, H. *Journal of Colloid and Interface Science* **2005**, *286*, 627–631.

(36) Pohl, A.; Dunn, B. *Thin Solid Films* **2006**, *515*, 790–792.

(37) Hou, K.; Puzzo, D.; Helander, M. G.; Lo, S. S.; Bonifacio, L. D.; Wang, W.; Lu, Z.; Scholes, G. D.; Ozin, G. A. *Advanced Materials* **2009**, *21*, 2492–2496.

(38) Wang, Y.; Brezesinski, T.; Antonietti, M.; Smarsly, B. *ACS Nano* **2009**, *3*, 1373–1378.

(39) O'Regan, B.; Grätzel, M. *Nature* **1991**, *353*, 737–740.

(40) Meng, Y.; Gu, D.; Zhang, F.; Shi, Y.; Yang, H.; Li, Z.; Yu, C.; Tu, B.; Zhao, D. *Angewandte Chemie International Edition* **2005**, *44*, 7053–7059.

(41) Meng, Y.; Gu, D.; Zhang, F.; Shi, Y.; Cheng, L.; Feng, D.; Wu, Z.; Chen, Z.; Wan, Y.; Stein, A.; Zhao, D. *Chemistry of Materials* **2006**, *18*, 4447–4464.

(42) Liang, C.; Li, Z.; Dai, S. *Angewandte Chemie International Edition* **2008**, *47*, 3696–3717.

(43) Zhang, F.; Meng, Y.; Gu, D.; Yan; Yu, C.; Tu, B.; Zhao, D. *J. Am. Chem. Soc.* **2005**, *127*, 13508–13509.

(44) Brezesinski, T.; Fischer, A.; Iimura, K. -i.; Sanchez, C.; Grosso, D.; Antonietti, M.; Smarsly, B. M. *Advanced Functional Materials* **2006**, *16*, 1433–1440.

(45) Han, S.; Hyeon, T. *Carbon* **1999**, *37*, 1645–1647.

(46) Han, S.; Sohn, K.; Hyeon, T. *Chemistry of Materials* **2000**, *12*, 3337–3341.

(47) Stein, A.; Schroden, R. C. *Current Opinion in Solid State and Materials Science* **2001**, *5*, 553–564.

(48) Baumann, T. F.; Satcher, J. *Journal of Non-Crystalline Solids* **2004**, *350*, 120–125.

(49) Holland, B. T.; Blanford, C. F.; Do, T.; Stein, A. *Chemistry of Materials* **1999**, *11*, 795–805.

(50) Arsenault, E.; Soheilnia, N.; Ozin, G. A. *ACS Nano* **2011**, *5*, 2984–2988.

(51) Kruk, M.; Jaroniec, M.; Ko, C. H.; Ryoo, R. *Chem. Mater.* **2000**, *12*, 1961–1968.

(52) Ding, S.; Wang, Z.; Madhavi, S.; Lou, X. W. *J. Mater. Chem.* **2011**, *21*, 13860–13864.

(53) Ramasamy, E.; Lee, J. *J. Phys. Chem. C* **2010**, *114*, 22032–22037.

(54) Smått, J.-H.; Weidenthaler, C.; Rosenholm, J. B.; Lindén, M. *Chem. Mater.* **2006**, *18*, 1443–1450.

(55) Jun, S.; Joo, S. H.; Ryoo, R.; Kruk, M.; Jaroniec, M.; Liu, Z.; Ohsuna, T.; Terasaki, O. *Journal of the American Chemical Society* **2000**, *122*, 10712–10713.

(56) Wijnhoven, J. E. G. J.; Vos, W. L. *Science* **1998**, *281*, 802–804.

(57) Cullity, B. D. *Elements of x-ray diffraction*; Addison-Wesley Pub. Co.: Reading, Mass., 1978.

(58) Azároff, L. V.; Buerger, M. J. *The powder method in X-ray crystallography*; McGraw-Hill, 1958.

(59) Kinoshita, K. *Carbon electrochem. and physicochem. properties.*; Wiley: New York, 1988.

(60) Biscoe, J.; Warren, B. E. *Journal of Applied Physics* **1942**, *13*, 364–371.

(61) Schrader, B.; Bougeard, D. *Infrared and Raman spectroscopy: methods and applications*; VCH: Weinheim; New York, 1995.

(62) Knight, D. S.; White, W. B. *J. Mater. Res.* **1989**, *4*, 385–393.

(63) Eklund, P. C.; Holden, J. M.; Jishi, R. A. *Carbon* **1995**, *33*, 959–972.

(64) Tuinstra, F.; Koenig, J. L. *The Journal of Chemical Physics* **1970**, *53*, 1126–1130.

(65) Brunauer, S.; Emmett, P. H.; Teller, E. *J. Am. Chem. Soc.* **1938**, *60*, 309–319.

(66) Barrett, E. P.; Joyner, L. G.; Halenda, P. P. *J. Am. Chem. Soc.* **1951**, *73*, 373–380.

(67) Lowell, S.; Shields, J.; Thomas, M.; Thommes, M. *Characterization of porous solids and powders: surface area, pore size, and density*; Kluwer Academic Publishers: Dordrecht; Boston, 2004.

(68) Conway, B. *Electrochemical Supercapacitors: Scientific Fundamentals and Technological Applications*; Plenum Press: New York, 1999.

(69) *Carbon Nanomaterials*; Gogotsi, Y.; Presser, V., Eds.; CRC Press, 2006.

(70) Frackowiak, E.; Béguin, F. *Carbon* **2001**, *39*, 937–950.

(71) Reimschuessel, A. C. *J. Chem. Educ.* **1972**, *49*, A413.

(72) Williams, D. B.; Carter, C. B. *Transmission electron microscopy. a textbook for materials science I, Basics*; Plenum Press: New York, 1996.

(73) Grätzel, M. *Journal of Sol-Gel Science and Technology* **2001**, *22*, 7–13.

(74) Franke, M. E.; Koplin, T. J.; Simon, U. *Small* **2006**, *2*, 301–301.

(75) Müller, V.; Rasp, M.; Rathouský, J.; Schütz, B.; Niederberger, M.; Fattakhova-Rohlfing, D. *Small* **2010**, *6*, 633–637.

(76) Thomas, A.; Schlaad, H.; Smarsly, B.; Antonietti, M. *Langmuir* **2003**, *19*, 4455–4459.

(77) Lu, A. ‐H.; Schüth, F. *Advanced Materials* **2006**, *18*, 1793–1805.

(78) Li, W.; Lu, A.; Schmidt, W.; Schüth, F. *Chemistry - A European Journal* **2005**, *11*, 1658–1664.

(79) Vendamme, R.; Onoue, S.-Y.; Nakao, A.; Kunitake, T. *Nat Mater* **2006**, *5*, 494–501.

(80) Leventis, N.; Chandrasekaran, N.; Sadekar, A. G.; Sotiriou-Leventis, C.; Lu, H. *Journal of the American Chemical Society* **2009**, *131*, 4576–4577.

(81) Leventis, N.; Chandrasekaran, N.; Sadekar, A. G.; Mulik, S.; Sotiriou-Leventis, C. *J. Mater. Chem.* **2010**, *20*, 7456.

(82) Halsey, G. *J. Chem. Phys.* **1948**, *16*, 931.

(83) Faass, G. S. Correlation of gas adsorption, mercury intrusion, and electron microscopy pore property data for porous glasses, Georgia Institute of Technology, 1981.

(84) Phillips, R. E.; Soulen, R. L. *Journal of Chemical Education* **1995**, *72*, 624.

(85) Baumann, T. F.; Gash, A. E.; Chinn, S. C.; Sawvel, A. M.; Maxwell, R. S.; Satcher, J. H. *Chemistry of Materials* **2005**, *17*, 395–401.

(86) Ladd, D. M.; Volosin, A.; Seo, D.-K. *J. Mater. Chem.* **2010**, *20*, 5923–5929.

(87) Baumann, T. F.; Worsley, M. A.; Han, T. Y.-J.; Satcher Jr., J. H. *Journal of Non-Crystalline Solids* **2008**, *354*, 3513–3515.

(88) Brandt, R.; Fricke, J. *Journal of Non-Crystalline Solids* **2004**, *350*, 131–135.

(89) Reuß, M.; Ratke, L. *Journal of Sol-Gel Science and Technology* **2008**, *47*, 74–80.

(90) Mulik, S.; Sotiriou-Leventis, C.; Leventis, N. *Chemistry of Materials* **2007**, *19*, 6138–6144.

(91) Liu, T. J.; Jin, Z. G.; Feng, L. R.; Wang, T. *Applied Surface Science* **2008**, *254*, 6547–6553.

(92) Müller, V.; Rasp, M.; Štefanić, G.; Ba, J.; Günther, S.; Rathousky, J.; Niederberger, M.; Fattakhova-Rohlfing, D. *Chemistry of Materials* **2009**, *21*, 5229–5236.

(93) Simmons, C. R.; Schmitt, D.; Wei, X.; Han, D.; Volosin, A. M.; Ladd, D. M.; Seo, D.-K.; Liu, Y.; Yan, H. *ACS Nano* **2011**, *5*, 6060–6068.

(94) Montilla, F.; Morallón, E.; De Battisti, A.; Barison, S.; Daolio, S.; Vázquez, J. L. *The Journal of Physical Chemistry B* **2004**, *108*, 15976–15981.

(95) Terrier, C.; Chatelon, J. P.; Berjoan, R.; Roger, J. A. *Thin Solid Films* **1995**, *263*, 37–41.

(96) Terrier, C.; Chatelon, J. P.; Roger, J. A.; Berjoan, R.; Dubois, C. *Journal of Sol-Gel Science and Technology* **1997**, *10*, 75–81.

(97) Fonstad, C. G.; Rediker, R. H. *Journal of Applied Physics* **1971**, *42*, 2911–2918.

(98) Nütz, T.; Felde, U. zum; Haase, M. *The Journal of Chemical Physics* **1999**, *110*, 12142–12150.

(99) Nütz, T.; Haase, M. *J. Phys. Chem. B* **2000**, *104*, 8430–8437.

(100) Qi, Z.; Honma, I.; Zhou, H. *Anal. Chem.* **2006**, *78*, 1034–1041.

(101) Farmer, J. C.; Fix, D. V.; Mack, G. V.; Pekala, R. W.; Poco, J. F. *J. Electrochem. Soc.* **1996**, *143*, 159–169.

(102) Pekala, R. W.; Farmer, J. C.; Alviso, C. T.; Tran, T. D.; Mayer, S. T.; Miller, J. M.; Dunn, B. *Journal of Non-Crystalline Solids* **1998**, *225*, 74–80.

(103) Braun, A.; Seifert, S.; Ilavsky, J. *Journal of Materials Research* **2010**, *25*, 1532–1540.

(104) Park, S.; Ruoff, R. S. *Nat Nano* **2009**, *4*, 217–224.

(105) Zhu, Y.; Murali, S.; Stoller, M. D.; Ganesh, K. J.; Cai, W.; Ferreira, P. J.; Pirkle, A.; Wallace, R. M.; Cychosz, K. A.; Thommes, M.; Su, D.; Stach, E. A.; Ruoff, R. S. *Science* **2011**, *332*, 1537 –1541.

(106) Guo, Y.; Qi, J.; Jiang, Y.; Yang, S.; Wang, Z.; Xu, H. *Materials Chemistry and Physics* **2003**, *80*, 704–709.

(107) Chmiola, J.; Yushin, G.; Gogotsi, Y.; Portet, C.; Simon, P.; Taberna, P. L. *Science* **2006**, *313*, 1760–1763.

(108) Merlet, C.; Rotenberg, B.; Madden, P. A.; Taberna, P.-L.; Simon, P.; Gogotsi, Y.; Salanne, M. *Nature Materials* **2012**, *11*, 306–310.

(109) Niu, J.; Pell, W. G.; Conway, B. E. *Journal of Power Sources* **2006**, *156*, 725–740.

(110) de Levie, R. *Electrochimica Acta* **1963**, *8*, 751–780.

(111) de Levie, R. *Electrochimica Acta* **1964**, *9*, 1231–1245.

(112) Yang, K.-L.; Yiacoumi, S.; Tsouris, C. *Journal of Electroanalytical Chemistry* **2003**, *540*, 159–167.

(113) Shopsowitz, K. E.; Hamad, W. Y.; MacLachlan, M. J. *Angewandte Chemie International Edition* **2011**, *50*, 10991–10995.

(114) Gash, A. E.; Tillotson, T. M.; Satcher; Poco, J. F.; Hrubesh, L. W.; Simpson, R. L. *Chemistry of Materials* **2001**, *13*, 999–1007.

(115) Gash, A. E.; Tillotson, T. M.; Satcher Jr., J. H.; Hrubesh, L. W.; Simpson, R. L. *Journal of Non-Crystalline Solids* **2001**, *285*, 22–28.

(116) Roelofs, F.; Vogelsberger, W. *Journal of colloid and interface science* **2006**, *303*, 450–459.

(117) Cançado, L. G.; Takai, K.; Enoki, T.; Endo, M.; Kim, Y. A.; Mizusaki, H.; Jorio, A.; Coelho, L. N.; Magalhães-Paniago, R.; Pimenta, M. A. *Applied Physics Letters* **2006**, *88*, 163106–163106–3.

(118) Ferrari, A. C. *Solid State Communications* **2007**, *143*, 47–57.

(119) Ferrari, A.; Robertson, J. *Phys. Rev. B* **2000**, *61*, 14095–14107.

(120) Stoller, M. D.; Ruoff, R. S. *Energy Environ. Sci.* **2010**, *3*, 1294–1301.

(121) Morishita, T.; Soneda, Y.; Tsumura, T.; Inagaki, M. *Carbon* **2006**, *44*, 2360–2367.

(122) Ruiz, V.; Blanco, C.; Granda, M.; Menéndez, R.; Santamaría, R. *Journal of Applied Electrochemistry* **2007**, *37*, 717–721.

(123) Randin, J.-P.; Yeager, E. *Journal of Electroanalytical Chemistry and Interfacial Electrochemistry* **1975**, *58*, 313–322.

(124) Barbieri, O.; Hahn, M.; Herzog, A.; Kötz, R. *Carbon* **2005**, *43*, 1303–1310.

(125) Gogotsi, Y.; Simon, P. *Science* **2011**, *334*, 917 –918.

(126) Laine, J.; Yunes, S. *Carbon* **1992**, *30*, 601–604.

(127) Guo, Y.; Rockstraw, D. A. *Microporous and Mesoporous Materials* **2007**, *100*, 12–19.

(128) Wu, D.; Fu, R.; Dresselhaus, M. S.; Dresselhaus, G. *Carbon* **2006**, *44*, 675–681.

(129) Zhao, C.; Wang, W.; Yu, Z.; Zhang, H.; Wang, A.; Yang, Y. *J. Mater. Chem.* **2010**, *20*, 976–980.

(130) Cao, L.; Kruk, M. *Adsorption* **2010**, *16*, 465–472.

(131) Jun, S.; Joo, S. H.; Ryoo, R.; Kruk, M.; Jaroniec, M.; Liu, Z.; Ohsuna, T.; Terasaki, O. *J. Am. Chem. Soc.* **2000**, *122*, 10712–10713.

(132) Gierszal, K. P.; Kim, T.-W.; Ryoo, R.; Jaroniec, M. *The Journal of Physical Chemistry B* **2005**, *109*, 23263–23268.

(133) Ryoo, R.; Joo, S. H.; Kruk, M.; Jaroniec, M. *Advanced Materials* **2001**, *13*, 677–681.

(134) Han, S.; Hyeon, T. *Chem. Commun.* **1999**, 1955–1956.

(135) Morris, C. A.; Anderson, M. L.; Stroud, R. M.; Merzbacher, C. I.; Rolison, D. R. *Science* **1999**, *284*, 622–624.

(136) Mewis, J.; Wagner, N. J. *Advances in Colloid and Interface Science* **2009**, *147-148*, 214–227.

(137) Pierre, A. Kluwer Academic Publishers: Boston, 1998; pp. 193–197, 203–204.

(138) Pek, Y. S.; Wan, A. C. A.; Shekaran, A.; Zhuo, L.; Ying, J. Y. *Nat Nano* **2008**, *3*, 671–675.

(139) Baumann, T. F.; Gash, A. E.; Chinn, S. C.; Sawvel, A. M.; Maxwell, R. S.; Satcher, J. H. *Chemistry of Materials* **2005**, *17*, 395–401.

(140) Rouquerol, J.; Avnir, D.; Fairbridge, C. W.; Everett, D. H.; Haynes, J. M.; Pernicone, N.; Ramsay, J. D. F.; Sing, K. S. W.; Unger, K. K. *Pure Appl. Chem.* **1994**, *66*, 1739–1758.

(141) Volosin, A. M.; Sharma, S.; Traverse, C.; Newman, N.; Seo, D.-K. *J. Mater. Chem.* **2011**, *21*, 13232–13240.

(142) Rouquerol, J.; Llewellyn, P.; Rouquerol, F. *Studies in surface science and catalysis* **2007**, *160*, 49–56.